

# Viscous vertex model for active epithelial tissues

Shao-Zhen Lin,<sup>1, 2, \*</sup> Sham Tlili,<sup>3</sup> and Jean-François Rupprecht<sup>4, 5, 6, †</sup>

<sup>1</sup>*Guangdong Provincial Key Laboratory of Magnetoelectric Physics and Devices,  
School of Physics, Sun Yat-sen University, Guangzhou 510275, China.*

<sup>2</sup>*Centre for Physical Mechanics and Biophysics, School of Physics,  
Sun Yat-sen University, Guangzhou 510275, China.*

<sup>3</sup>*Aix Marseille Univ, CNRS and Turing Centre for Living Systems, IBMD, Marseille, 13009 (France).*

<sup>4</sup>*Aix Marseille Univ, CNRS and Turing Centre for Living Systems,  
Centre de Physique Théorique (UMR 7332), Marseille, 13009 (France).*

<sup>5</sup>*Aix Marseille Univ, CNRS and Turing Centre for Living Systems,  
Laboratoire Adhésion Inflammation (UMR 7333), 13009 (France).*

<sup>6</sup>*Aix Marseille Univ, Université de Toulon, CNRS, LAI (UMR 7333),  
Turing Centre for Living Systems, Marseille, France*

(Dated: February 16, 2026)

We present a rotationally invariant viscous vertex model that accounts for both cortical and bulk dissipations of cells. The vanishing substrate-friction limit is enforced via Lagrange multipliers, which also provide a route to strongly constrained boundary conditions such as fixed boundaries and prescribed tractions. Building on this formulation, we introduce a slab-shear rheology protocol to extract an effective, coarse-grained tissue shear viscosity. Under polar or nematic activity, viscosity regulates the formation of elongated, spatially correlated cell-shape textures and stabilizes well-defined topological defects. Because the model remains well-posed at zero substrate friction, it is naturally suited to describing free-floating epithelia and organoids.

## I. INTRODUCTION

Confluent epithelial monolayers and other dense cell assemblies behave as active viscoelastic materials [1–7]. On short time scales ( $\lesssim 1$  s), cell junctions and cortical networks respond elastically to imposed deformations and forces, whereas over minutes, junctional crosslinkers turnover and actomyosin structures remodel, enabling sustained cortical flows under applied stresses [1, 8–11]. This rheological behavior underpins a wide range of morphogenetic processes and collective cell migration phenomena [3, 10, 12]. It is often described at a continuum scale within active polar/nematic gel frameworks, where effective viscosities and active stresses are introduced phenomenologically [13–15].

Cell-based models, particularly vertex models, provide a complementary and more microscopic description of tissue mechanics. In standard vertex models, cells are represented as polygons (Fig. 1(a)) whose vertices move in an overdamped manner in response to forces derived from area and perimeter elastic energies, together with prescribed cell-cell interfacial tensions [16–22]. Dissipation is commonly modeled as a local friction between vertices and a static mechanical support, such as the extracellular matrix or a rigid substrate [23]. In this widely used formulation, the junctional cortex is effectively treated as an elastic element, while viscous contributions to junctional tension are neglected.

Yet internal viscous forces seem to dominate over ex-

ternal friction in several systems, e.g., within free-floating embryonic tissues and free-standing monolayers [24–26]. In the *Drosophila* embryo, estimates of tissue flows and force balances indicate that specific friction against the surrounding medium is often small compared to bulk and cortical viscosity [27, 28]. At the cellular level, the actomyosin cortex is significantly more viscous than the cytoplasm: despite its small thickness (typically  $\ell_{\text{cortex}} \simeq 0.2 \mu\text{m}$  compared to a cytoplasmic scale  $\ell_{\text{cyt}} \simeq 5 \mu\text{m}$ ), the cortex can provide the dominant contribution to dissipation [11, 29–31]. This motivates explicit models of junctional viscosity.

A series of pioneering continuum and cell-based studies incorporated cell bulk viscosity while keeping junctional tensions fixed [32, 33], hence accounting for such a large difference in apparent viscosities between bulk and cortex. A recent set of papers then accounted for the possibility of a viscous cortical response, either to describe cell division and apoptosis in suspended monolayers [34], spatial ordering in the *Xenopus* embryo [35], or the emergence of spontaneous shear flows in monolayers [3, 36, 37].

Despite these advances, we still lack a systematic formulation of a viscous vertex model that (i) treats both junctional and bulk viscosities of cells on the same footing, (ii) remains rotationally invariant and independent of arbitrary reference frames, (iii) is well-posed in the limit of vanishing substrate friction, and (iv) yields a clear coarse-grained tissue viscosity.

In this article, we develop a viscous extension of the vertex model that explicitly accounts for both cell-cell interfacial viscosity (i.e., junctional viscosity) and intracellular viscous drag between vertices and cell centers (mimicking cellular bulk viscosity), referred to as the *viscous vertex model*. Junctional viscosity is introduced through

\*Electronic address: [linshaozhen@mail.sysu.edu.cn](mailto:linshaozhen@mail.sysu.edu.cn)

†Electronic address: [jean-francois.rupprecht@univ-amu.fr](mailto:jean-francois.rupprecht@univ-amu.fr)

velocity differences projected along edges, and bulk viscosity through relative motion between vertices and cell geometric centers, resulting in a rotationally invariant, frame-independent formulation. The resulting force balance can be written in the following matrix form,

$$\mathbf{C} \cdot \mathbf{v} = \mathbf{F}^{(t)}, \quad (1)$$

where  $\mathbf{C}$  is a friction–viscosity coefficient matrix combining substrate friction, junctional viscosity, and bulk viscosity;  $\mathbf{v}$  collects all vertex velocities;  $\mathbf{F}^{(t)}$  gathers all non-dissipative forces (e.g., elastic forces and active forces).

Our framework tackles situations in which the friction between cells and their environment is negligible, such as free-floating tissues [24, 26] and organoids [12, 38]. As pointed out in Ref. [23], in this limit, the coefficient matrix  $\mathbf{C}$  in Eq. (1) becomes singular because global translations and rotations are unconstrained. This difficulty is resolved by (1) taking into account a finite bulk viscosity and (2) imposing global or boundary kinematic constraints via a Lagrange multiplier formalism. These two operations regularize the linear system and enable simulations at strictly zero friction. The same approach is used to implement prescribed boundary conditions, including dragging a single cell or a cell cluster, fixed or freely sliding boundaries in a confinement geometry (e.g., slab, disk, ring geometries), and external pulling protocols.

Within this framework, we introduce a slab-shear protocol to measure a coarse-grained tissue viscosity directly from vertex velocities and line tensions. In the absence of activity, we extract a short-time tissue viscosity from the instantaneous linear relationship between viscous shear stress and imposed shear strain rate. We derive an analytical expression for the short-time viscosity in the case of a tissue formed of regularly packed hexagonal cells, and find that it scales linearly with the junctional and bulk viscosities even at relatively large values. Numerical simulations confirm that this relation holds in disordered cell packings. Allowing for cell rearrangements under sustained shear, we then extract a long-time tissue viscosity, which we also find to scale linearly with the junctional and bulk viscosities.

Finally, the consequences of cellular viscosity are explored in two typical kinds of active vertex models: (1) a polar active vertex model, which accounts for polar active traction forces at the leading edge of cells; (2) a nematic active vertex model, which implements cell-shape-dependent active stresses. Both kinds of cellular activities drive flows and the dynamics of topological defects. Increasing junctional and bulk viscosities leads to more elongated and spatially correlated cell shapes, modifies the density and organization of  $\pm 1/2$  topological defects, and promotes coherent flow structures in both periodic domains and confined geometries. Because the formulation remains well-posed as the substrate friction vanishes, it is directly applicable to free-floating tissues and organoids, thereby providing a bridge between cell-

based models and continuum active nematic descriptions of living tissues.

## II. A ROTATION-INVARIANT FORMULATION OF DISSIPATION AT CELL-CELL INTERFACES

### A. Implementation of cellular viscosities

#### 1. Cell-cell interfacial viscosity

Besides the usually considered constant cell–cell interfacial tension, in the general case, here, we also consider the viscosity of intercellular junctions, as shown in Fig. 1(b). Assuming a linear relation between the cell–cell interfacial viscous tension and the cell–cell interfacial elongation rate, we express the viscous tension  $\Lambda_{ij}^{(\text{viscous})}$  of the cell–cell interface  $ij$  as,

$$\Lambda_{ij}^{(\text{viscous})} = \eta_{ij}^{(s)} \dot{l}_{ij}, \quad (2)$$

where  $l_{ij} = |\mathbf{r}_i - \mathbf{r}_j|$  is the length of the cell–cell interface  $ij$ , and  $\dot{l}_{ij} = dl_{ij}/dt$  is corresponding elongation rate;  $\eta_{ij}^{(s)}$  is the viscous coefficient of the cell–cell interface  $ij$  (different from traditional fluid viscosity). Since  $\dot{l}_{ij} = dl_{ij}/dt = d(|\mathbf{r}_i - \mathbf{r}_j|)/dt = \mathbf{t}_{i,j} \cdot (\mathbf{v}_j - \mathbf{v}_i)$  with  $\mathbf{t}_{i,j} = (\mathbf{r}_j - \mathbf{r}_i)/l_{ij}$ , the cell–cell interfacial viscous tension can be re-expressed as,

$$\Lambda_{ij}^{(\text{viscous})} = \eta_{ij}^{(s)} \mathbf{t}_{i,j} \cdot (\mathbf{v}_j - \mathbf{v}_i). \quad (3)$$

Note that there exist different ways to define the cell–cell interfacial viscous tension  $\Lambda_{ij}^{(\text{viscous})}$ . An alternative, rotation-invariant definition could be  $\Lambda_{ij}^{(\text{viscous})} = \eta_{ij}^{(s)} \dot{\varepsilon}_{ij}$ , which relies on the cell–cell interface elongation strain rate  $\dot{\varepsilon}_{ij} = \dot{l}_{ij}/l_{ij}$  with  $\varepsilon_{ij} = \ln(l_{ij}/l_{ij,0})$  being the logarithmic strain of the cell–cell interface  $ij$ . In Sec. II A 3, we demonstrate that such a definition tends to suppress T1 topological transitions. Thus, we focus on the viscous tension definition in Eq. (3) hereafter.

Further considering the tension fluctuations, the total interfacial tension  $\Lambda_{ij}$  of the cell–cell interface  $ij$  can be expressed as (Fig. 1(c)),

$$\Lambda_{ij} = \eta_{ij}^{(s)} \mathbf{t}_{i,j} \cdot (\mathbf{v}_j - \mathbf{v}_i) + \Lambda_{ij}^{(0)} + \frac{1}{\sqrt{l_{ij}}} \zeta_{ij}, \quad (4)$$

where  $\Lambda_{ij}^{(0)}$  is the normal tension of the cell–cell interface  $ij$  in the case of no viscosity and no fluctuations;  $\zeta_{ij}$  is the stochastic fluctuations of the cell–cell interfacial tension.

#### 2. Cell bulk viscosity

In addition to the cell–cell interfacial viscosity, we also consider the bulk viscosity of cells, as shown in Fig. 1(b). Assuming a linear relation between the viscous cell–bulk

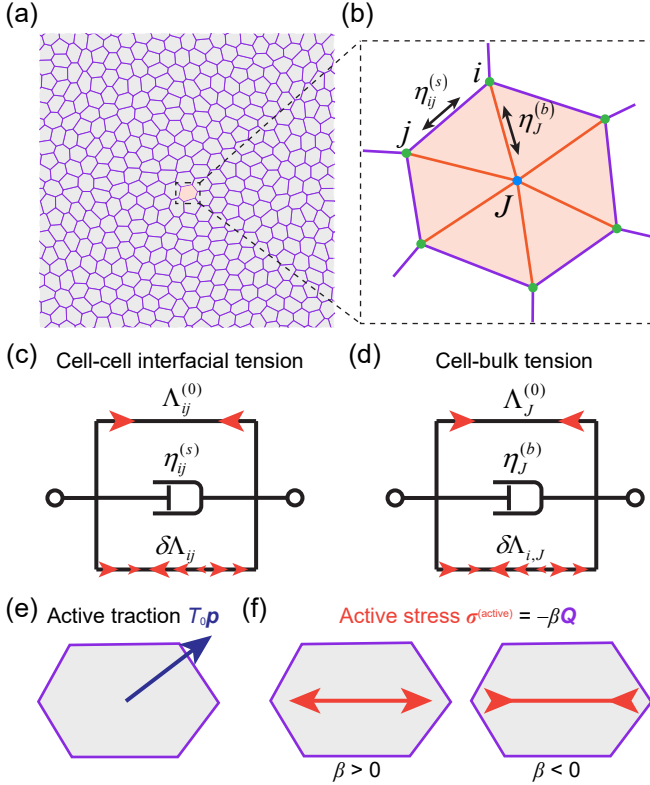


FIG. 1: Schematic of the active, viscous vertex model. (a) In vertex models, a cell sheet is mimicked by a tilting of polygons. (b) Schematic of the two kinds of cellular viscosities considered in our model, including the cell-cell interfacial viscosity ( $\eta_{ij}^{(s)}$ ) and the cell cytoplasm viscosity ( $\eta_J^{(b)}$ ). (c) Schematic of the cell-cell interfacial tension of the interface  $ij$ , including three contributions: (1) a constant tension  $\Lambda_{ij}^{(0)}$ ; (2) a viscous tension  $\eta_{ij}^{(s)}\dot{l}_{ij}$ ; (3) tension fluctuations  $\delta\Lambda_{ij}$ . (d) Schematic of the cell-bulk line tension of the segment  $iJ$ , including three contributions: (1) a constant tension  $\Lambda_J^{(0)}$ ; (2) a viscous tension  $\eta_J^{(b)}\dot{l}_{i,J}$ ; (3) tension fluctuations  $\delta\Lambda_{i,J}$ . (e) Schematic of the polar active traction force  $\mathbf{F}_J^{(\text{active})} = T_0 \mathbf{p}_J$  with  $T_0$  being the active traction magnitude and  $\mathbf{p}_J$  the cell polarization vector. (f) Schematic of the apolar active stress  $\sigma_J^{(\text{active})} = -\beta \mathbf{Q}_J$  with  $\beta$  being the cellular activity parameter and  $\mathbf{Q}_J$  the cell shape anisotropy tensor.

line tension and the vertex-cell center expansion rate, in a similar way, we can express the viscous cell-bulk line tension as,

$$\Lambda_{i,J}^{(\text{viscous})} = \eta_J^{(b)} \mathbf{t}_{i,J} \cdot (\mathbf{v}_J - \mathbf{v}_i), \quad (5)$$

where  $\Lambda_{i,J}^{(\text{viscous})}$  is the viscous line tension between vertex  $i$  and its neighboring cell  $J$ ;  $\eta_J^{(b)}$  is the bulk viscous coefficient of cell  $J$ ;  $\mathbf{t}_{i,J} = (\mathbf{r}_J - \mathbf{r}_i)/l_{i,J}$  with  $l_{i,J} = |\mathbf{r}_i - \mathbf{r}_J|$  being the distance of vertex  $i$  to the geometric center  $\mathbf{r}_J = \sum_{j \in \text{cell } J} \mathbf{r}_j/n_J$  of its neighboring cell  $J$ ;  $\mathbf{v}_J = d\mathbf{r}_J/dt$  is the velocity of the geometric center of cell  $J$ .

Similarly, considering the constant part and fluctua-

tions, the total tension of cell vertices to the cell center can be expressed as (Fig. 1(d)),

$$\Lambda_{i,J} = \eta_J^{(b)} \mathbf{t}_{i,J} \cdot (\mathbf{v}_J - \mathbf{v}_i) + \Lambda_J^{(0)} + \frac{1}{\sqrt{l_{i,J}}} \zeta_{i,J}, \quad (6)$$

where  $\Lambda_J^{(0)}$  is the normal line tension between vertex  $i$  and its neighboring cell  $J$  in the case of no bulk viscosity and no stochastic fluctuations;  $\zeta_{i,J}$  is the stochastic fluctuations of the cell-bulk line tension. Since  $\mathbf{v}_J = d\mathbf{r}_J/dt = \sum_{j \in \text{cell } J} \mathbf{v}_j/n_J$ , Eq. (6) can be further expressed as,

$$\begin{aligned} \Lambda_{i,J} &= \eta_J^{(b)} \mathbf{t}_{i,J} \cdot \left( \frac{1}{n_J} \sum_{j \in \text{cell } J} \mathbf{v}_j - \mathbf{v}_i \right) + \Lambda_J^{(0)} + \frac{1}{\sqrt{l_{i,J}}} \zeta_{i,J} \\ &= \eta_J^{(b)} \mathbf{t}_{i,J} \cdot \left( -\frac{n_J - 1}{n_J} \mathbf{v}_i + \frac{1}{n_J} \sum_{j \in \text{cell } J, j \neq i} \mathbf{v}_j \right) \\ &\quad + \Lambda_J^{(0)} + \frac{1}{\sqrt{l_{i,J}}} \zeta_{i,J}. \end{aligned} \quad (7)$$

### 3. Discussion: an alternative formulation of viscous tension

Here, we provide an alternative, rotation-invariant definition of the cell-cell interfacial viscous tension:

$$\Lambda_{ij}^{(\text{viscous})} = \eta_{ij}^{(s)} \dot{\varepsilon}_{ij}, \quad (8)$$

where  $\dot{\varepsilon}_{ij}$  quantifies the elongation/shrinkage strain of the cell-cell interface  $ij$ . Since cell-cell interfaces can undergo large elongation or shrinkage, we employ the logarithmic strain to quantify the elongation/shrinkage of cell-cell interfaces, i.e.,

$$\varepsilon_{ij} = \ln \left( \frac{l_{ij}}{l_{ij,0}} \right), \quad (9)$$

where  $l_{ij,0}$  refers to a rest-length parameter of the cell-cell interface  $ij$ . From Eq. (9), we obtain that  $\dot{\varepsilon}_{ij} = \dot{l}_{ij}/l_{ij}$ . Then, Eq. (8) further reads,

$$\Lambda_{ij}^{(\text{viscous})} = \eta_{ij}^{(s)} \frac{\dot{l}_{ij}}{l_{ij}}. \quad (10)$$

Thus, the total cell-cell interfacial tension reads,

$$\Lambda_{ij} = \eta_{ij}^{(s)} \frac{\dot{l}_{ij}}{l_{ij}} + \Lambda_{ij}^{(0)} + \frac{1}{\sqrt{l_{ij}}} \zeta_{ij}. \quad (11)$$

Examining the cell-cell interfacial viscosity term, it suggests that if any cell-cell interface  $ij$  shrinks to very short, i.e.,  $l_{ij} \rightarrow 0$  and  $\dot{l}_{ij} < 0$ , which decreases the cell-cell interfacial tension and even leads to a negative value, the shrinkage of the cell-cell interface will thus be resisted. This can be further directly illustrated by

considering the 1D case. Setting  $\Lambda_{ij} = 0$  and ignoring stochastic fluctuations, Eq. (11) reads,

$$\dot{l}_{ij} = -\frac{\Lambda_{ij}^{(0)}}{\eta_{ij}^{(s)}} l_{ij}, \quad (12)$$

which leads to,

$$l_{ij}(t) = l_{ij,0} \exp \left[ -\frac{\Lambda_{ij}^{(0)}}{\eta_{ij}^{(s)}} t \right], \quad (13)$$

where  $l_{ij,0} = l_{ij}(t = 0)$  here. The above equation clearly shows that an increase in the cell-cell interfacial viscosity  $\eta_{ij}^{(s)}$  slows the shrinkage of the cell-cell interface. Therefore, the cell-cell interfacial viscosity defined in Eq. (8) tends to suppress T1 topological transitions, that is, cell neighbor exchange [16, 19]. In comparison, with the definition of Eq. (2), one can obtain  $l_{ij}(t) = l_{ij,0} - [\Lambda_{ij}^{(0)} / \eta_{ij}^{(s)}]t$ , which results in a finite shrinkage time of cell-cell interface. In this study, we adopt the definition in Eq. (2) rather than Eq. (8) for the viscous tension.

## B. Motion equation

### 1. Force balance

The dynamics of the cell sheet can be characterized by the motion of vertices, i.e.,  $\mathbf{r}_i(t)$  with  $i = 1, 2, \dots, N_v$  being the index of vertices and  $N_v$  the total number of vertices. In general, the force balance at vertex  $i$  can be decomposed into three generic terms:

$$\mathbf{F}_i^{(\text{elastic})} + \mathbf{F}_i^{(\text{active})} + \mathbf{F}_i^{(\text{dissipation})} = \mathbf{0}, \quad (14)$$

each corresponding to the elastic forces associated with cell shape regulation, to active force generating motion and cell deformation, and to dissipation resisting motion and cell shape elongation (cell-substrate friction, cell-cell interfacial tension, and cell bulk tension), respectively. We detail the specific expression of each term within the next paragraphs.

*Elastic forces.* – We decompose the elastic cell shape relaxation force into two contributions:

$$\mathbf{F}_i^{(\text{elastic})} = \mathbf{F}_i^{(\text{area})} + \mathbf{F}_i^{(\text{perimeter})}, \quad (15)$$

which can be obtained by taking the partial derivatives ( $\partial / \partial \mathbf{r}_i$ ) of the corresponding mechanical energy of the cell sheet [16–22, 39], i.e.,  $\mathbf{F}_i^{(\text{area})} = -\partial E_{\text{area}} / \partial \mathbf{r}_i$  and  $\mathbf{F}_i^{(\text{perimeter})} = -\partial E_{\text{perimeter}} / \partial \mathbf{r}_i$ . Specifically, the mechanical energy of cell area elasticity can be expressed as,

$$E_{\text{area}} = \sum_{j=1}^{N_c} \frac{1}{2} K_A (A_J - A_0)^2, \quad (16)$$

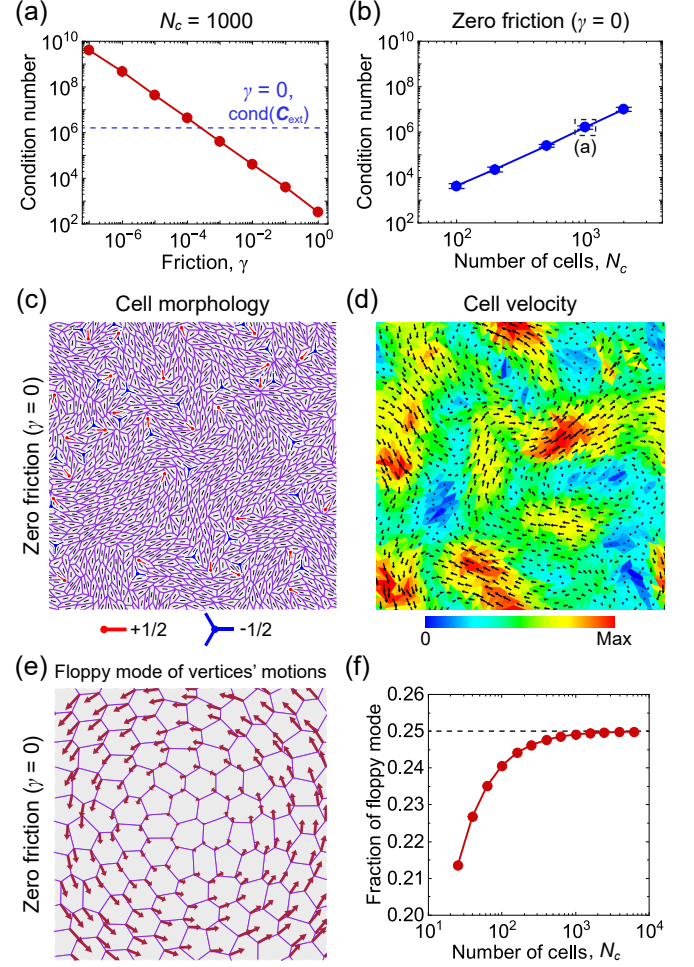


FIG. 2: Numerical simulation of an active cell sheet in a square domain with periodic boundary conditions. Here, we consider cell-shape-dependent active stresses; see Sec. IV C. (a) The condition number of the friction-viscosity coefficient matrix  $\mathbf{C}$  as a function of the friction  $\gamma$ , for a system consisting of  $N_c = 10^3$  cells. The dashed blue line represents the condition number of the extended viscosity coefficient matrix  $\mathbf{C}_{\text{ext}}$  (see Eq. (47)). Data analysis gives a scaling law,  $\text{cond}(\mathbf{C}) \sim \gamma^{-1}$ . (b-d) The case without friction ( $\gamma = 0$ ), using the protocol proposed in Sec. II C 2. (b) The condition number of the extended viscosity coefficient matrix  $\mathbf{C}_{\text{ext}}$  (see Eq. (47)) as a function of the number of cells  $N_c$ . Data analysis gives a scaling law,  $\text{cond}(\mathbf{C}_{\text{ext}}) \sim N_c^\alpha$  with  $\alpha \approx 2.6$ . (c) A typical cell morphology. The black lines indicate cell orientations; the red (resp. blue) symbols represent  $+1/2$  (resp.  $-1/2$ ) topological defects, extracted using the scheme proposed in Ref. [21]. (d) A typical flow field, where the black arrows represent the velocity vectors and the color code refers to the velocity magnitude. (e, f) Floppy modes of vertices' motions in the case of no friction ( $\gamma = 0$ ) and no bulk viscosity ( $\eta_b = 0$ ). (e) Illustration of a typical floppy mode in a cell layer consisting of  $N_c = 100$  cells, obtained by numerical calculation of Eq. (48). The arrows represent the vertices' velocity vectors. (f) The fraction of floppy modes  $f$  as a function of the number of cells  $N_c$ . Parameters:  $\eta_s = 10$ ,  $T_0 = 0$ , and  $\beta = 0.4$ ;  $\eta_b = 10$  for (a-d).

where  $K_A$  is the area elastic moduli of cells,  $A_0$  is a preferred cell area, and  $A_J$  is the area of the  $J$ -th cell; the summation  $\sum_{J=1}^{N_c}$  is made over all cells indexed by  $J = 1, 2, \dots, N_c$  with  $N_c$  being the total number of cells. The mechanical energy of cell perimeter elasticity can be expressed as,

$$E_{\text{perimeter}} = \sum_{J=1}^{N_c} \frac{1}{2} K_P (P_J - P_0)^2, \quad (17)$$

where  $K_P$  is the perimeter elastic moduli of cells,  $P_0$  is a preferred cell perimeter, and  $P_J$  is the perimeter of the  $J$ -th cell.

*Active forces.* – The active force  $\mathbf{F}_i^{(\text{active})}$  accounts for forces related to the activity of cells, which typically includes two kinds (Fig. 1(e,f)), i.e., the polar active traction force mimicking the activity of cell protrusions at the leading edge of cells [19, 40–44] and the apolar active cellular stress mimicking the contractility/extensibility of the intracellular cytoskeleton [21, 36, 37, 39, 45–47]. We discuss in details several models for the active force  $\mathbf{F}_i^{(\text{active})}$  in Sec. IV B and IV C.

*Dissipation.* – We will consider three forces contributing to dissipation:

$$\mathbf{F}_i^{(\text{dissipation})} = \mathbf{F}_i^{(\text{friction})} + \mathbf{F}_i^{(\text{interface})} + \mathbf{F}_i^{(\text{bulk})}, \quad (18)$$

each corresponding to cell–substrate friction, cell–cell interfacial tension, and cell bulk tension, in turn.

We assume a linear relation between the friction  $\mathbf{F}_i^{(\text{friction})}$  and the vertex motion velocity  $\mathbf{v}_i = d\mathbf{r}_i/dt$ , the friction force can be expressed as,  $\mathbf{F}_i^{(\text{friction})} = -\gamma_i \cdot \mathbf{v}_i$  with  $\gamma_i$  being the 2D tensor friction coefficient between the vertex  $i$  and the substrate. In general,  $\gamma_i$  can depend on cell shape and the substrate patterns. In the isotropic case,  $\gamma_i = \gamma_i \mathbf{I}$  with  $\gamma_i$  being a scalar friction coefficient and  $\mathbf{I}$  the second-order unit tensor.

Considering the cell–cell interfacial tension and cell bulk tension as described in Sec. II A, we obtain the detailed expressions of  $\mathbf{F}_i^{(\text{interface})}$  and  $\mathbf{F}_i^{(\text{bulk})}$  as below:

$$\begin{aligned} \mathbf{F}_i^{(\text{interface})} &= \sum_{j \in V_i} \Lambda_{ij} \mathbf{t}_{i,j} \\ &= - \sum_{j \in V_i} \eta_{ij}^{(s)} (\mathbf{t}_{i,j} \otimes \mathbf{t}_{i,j}) \cdot \mathbf{v}_i \\ &\quad + \sum_{j \in V_i} \eta_{ij}^{(s)} (\mathbf{t}_{i,j} \otimes \mathbf{t}_{i,j}) \cdot \mathbf{v}_j \\ &\quad + \mathbf{F}_i^{(s0)}, \end{aligned} \quad (19)$$

and

$$\begin{aligned} \mathbf{F}_i^{(\text{bulk})} &= \sum_{J \in C_i} \Lambda_{i,J} \mathbf{t}_{i,J} \\ &= - \sum_{J \in C_i} \left( \eta_J^{(b)} \frac{n_J - 1}{n_J} \mathbf{t}_{i,J} \otimes \mathbf{t}_{i,J} \right) \cdot \mathbf{v}_i \\ &\quad + \sum_{J \in C_i} \left( \eta_J^{(b)} \frac{1}{n_J} \mathbf{t}_{i,J} \otimes \mathbf{t}_{i,J} \right) \cdot \sum_{\substack{j \in \text{cell } J \\ j \neq i}} \mathbf{v}_j \\ &\quad + \mathbf{F}_i^{(b0)}, \end{aligned} \quad (20)$$

where

$$\mathbf{F}_i^{(s0)} = \sum_{j \in V_i} \left( \Lambda_{ij}^{(0)} + \frac{1}{\sqrt{l_{ij}}} \zeta_{ij} \right) \mathbf{t}_{i,j}, \quad (21)$$

and

$$\mathbf{F}_i^{(b0)} = \sum_{J \in C_i} \left( \Lambda_J^{(0)} + \frac{1}{\sqrt{l_{i,J}}} \zeta_{i,J} \right) \mathbf{t}_{i,J}, \quad (22)$$

are vertex velocity-independent cell–cell interfacial tension and cell–bulk tension;  $V_i$  and  $C_i$  are the set of neighboring vertices and neighboring cells of vertex  $i$ .

## 2. Matrix formalism of motion equation

Equation (14) gives the motion equation of each vertex  $i$ . Here, we further express it in detail. Substituting Eqs. (19) and (20) into Eq. (14), we obtain

$$\begin{aligned} &\left[ \gamma_i + \sum_{j \in V_i} \eta_{ij}^{(s)} (\mathbf{t}_{i,j} \otimes \mathbf{t}_{i,j}) \right. \\ &\quad \left. + \sum_{J \in C_i} \left( \eta_J^{(b)} \frac{n_J - 1}{n_J} \mathbf{t}_{i,J} \otimes \mathbf{t}_{i,J} \right) \right] \cdot \mathbf{v}_i \\ &\quad - \sum_{j \in V_i} \eta_{ij}^{(s)} (\mathbf{t}_{i,j} \otimes \mathbf{t}_{i,j}) \cdot \mathbf{v}_j \\ &\quad - \sum_{J \in C_i} \left( \eta_J^{(b)} \frac{1}{n_J} \mathbf{t}_{i,J} \otimes \mathbf{t}_{i,J} \right) \cdot \sum_{\substack{j \in \text{cell } J \\ j \neq i}} \mathbf{v}_j = \mathbf{F}_i^{(t)}, \end{aligned} \quad (23)$$

where

$$\begin{aligned} \mathbf{F}_i^{(t)} &= \mathbf{F}_i^{(\text{area})} + \mathbf{F}_i^{(\text{perimeter})} + \mathbf{F}_i^{(\text{active})} \\ &\quad + \mathbf{F}_i^{(s0)} + \mathbf{F}_i^{(b0)}, \end{aligned} \quad (24)$$

is the total non-dissipative vertex force that is independent of cell vertex velocity. The matrix form of Eq. (23) reads,

$$\sum_{j=1}^{N_v} \mathbf{C}_{ij} \cdot \mathbf{v}_j = \mathbf{F}_i^{(t)}, \quad (25)$$

where

$$\mathbf{C}_{ij} = \mathbf{C}_{ij}^{(f)} + \mathbf{C}_{ij}^{(s)} + \mathbf{C}_{ij}^{(b)}. \quad (26)$$

Here,  $\mathbf{C}_{ij}^{(f)}$ ,  $\mathbf{C}_{ij}^{(s)}$  and  $\mathbf{C}_{ij}^{(b)}$  are the coefficient matrices of size  $2 \times 2$ , corresponding to the cell–substrate friction, the cell–cell interfacial viscosity and the cell bulk viscosity, with the detailed expression as below:

$$\mathbf{C}_{ij}^{(f)} = \gamma_i \delta_{ij} \quad (27)$$

$$\mathbf{C}_{ij}^{(s)} = \begin{cases} \sum_{k \in V_i} \eta_{ik}^{(s)} (\mathbf{t}_{i,k} \otimes \mathbf{t}_{i,k}) & , \quad j = i \\ -\eta_{ij}^{(s)} (\mathbf{t}_{i,j} \otimes \mathbf{t}_{i,j}) & , \quad j \in V_i \\ \mathbf{0} & , \quad \text{otherwise} \end{cases} \quad (28)$$

$$\mathbf{C}_{ij}^{(b)} = \begin{cases} \sum_{J \in C_i} \eta_J^{(b)} \frac{(n_J - 1)}{n_J} (\mathbf{t}_{i,J} \otimes \mathbf{t}_{i,J}) & , \quad j = i \\ -\sum_{i,j \in \text{cell } J} \eta_J^{(b)} \frac{1}{n_J} \mathbf{t}_{i,J} \otimes \mathbf{t}_{i,J} & , \quad j \neq i \\ \mathbf{0} & , \quad \text{otherwise} \end{cases} \quad (29)$$

Equation (25) gives the force balance at each vertex  $i$ ; totally, there are  $N_v$  force balance equations. We can further express all the force balance equations in a unified matrix form, as shown in Eq. (1). Note that for the general case, the force vector  $\mathbf{F}^{(t)}$  is not limited to the forces demonstrated above, but instead can include all kinds of cell velocity-independent forces.  $\mathbf{C}$ ,  $\mathbf{v}$  and  $\mathbf{F}^{(t)}$  are organized by  $\mathbf{C}_{ij}$ ,  $\mathbf{v}_i$  and  $\mathbf{F}_i$  as below:

$$\mathbf{C} = (\mathbf{C}_{ij})_{2N_v \times 2N_v} = \begin{pmatrix} \mathbf{C}_{11} & \dots & \mathbf{C}_{1N_v} \\ \vdots & \ddots & \vdots \\ \mathbf{C}_{N_v 1} & \dots & \mathbf{C}_{N_v N_v} \end{pmatrix}_{2N_v \times 2N_v} \quad (30)$$

$$\mathbf{v} = (\mathbf{v}_i)_{2N_v \times 1} = \begin{pmatrix} \mathbf{v}_1 \\ \vdots \\ \mathbf{v}_{N_v} \end{pmatrix}_{2N_v \times 1} \quad (31)$$

$$\mathbf{F}^{(t)} = (\mathbf{F}_i^{(t)})_{2N_v \times 1} = \begin{pmatrix} \mathbf{F}_1^{(t)} \\ \vdots \\ \mathbf{F}_{N_v}^{(t)} \end{pmatrix}_{2N_v \times 1} \quad (32)$$

The friction-viscosity coefficient matrix  $\mathbf{C}$  can be further decomposed as,

$$\mathbf{C} = \mathbf{C}^{(f)} + \mathbf{C}^{(s)} + \mathbf{C}^{(b)}, \quad (33)$$

where  $\mathbf{C}^{(f)}$ ,  $\mathbf{C}^{(s)}$  and  $\mathbf{C}^{(b)}$  are the friction coefficient matrix, the cell–cell interfacial viscosity coefficient matrix and the cell bulk viscosity coefficient matrix:

$$\begin{aligned} \mathbf{C}^{(f)} = (\mathbf{C}_{ij}^{(f)}) &= \begin{pmatrix} \mathbf{C}_{11}^{(f)} & \dots & \mathbf{C}_{1N_v}^{(f)} \\ \vdots & \ddots & \vdots \\ \mathbf{C}_{N_v 1}^{(f)} & \dots & \mathbf{C}_{N_v N_v}^{(f)} \end{pmatrix}_{2N_v \times 2N_v} \\ &= \begin{pmatrix} \gamma_1 & \dots & \mathbf{0} \\ \vdots & \ddots & \vdots \\ \mathbf{0} & \dots & \gamma_{N_v} \end{pmatrix}_{2N_v \times 2N_v} \end{aligned} \quad (34)$$

$$\mathbf{C}^{(s)} = (\mathbf{C}_{ij}^{(s)}) = \begin{pmatrix} \mathbf{C}_{11}^{(s)} & \dots & \mathbf{C}_{1N_v}^{(s)} \\ \vdots & \ddots & \vdots \\ \mathbf{C}_{N_v 1}^{(s)} & \dots & \mathbf{C}_{N_v N_v}^{(s)} \end{pmatrix}_{2N_v \times 2N_v} \quad (35)$$

$$\mathbf{C}^{(b)} = (\mathbf{C}_{ij}^{(b)}) = \begin{pmatrix} \mathbf{C}_{11}^{(b)} & \dots & \mathbf{C}_{1N_v}^{(b)} \\ \vdots & \ddots & \vdots \\ \mathbf{C}_{N_v 1}^{(b)} & \dots & \mathbf{C}_{N_v N_v}^{(b)} \end{pmatrix}_{2N_v \times 2N_v} \quad (36)$$

Note that,  $[\mathbf{C}_{ij}^{(s)}]^T = \mathbf{C}_{ij}^{(s)} = \mathbf{C}_{ji}^{(s)}$  and  $[\mathbf{C}_{ij}^{(b)}]^T = \mathbf{C}_{ij}^{(b)} \neq \mathbf{C}_{ji}^{(b)}$ . Thus, the cell–cell interfacial viscosity coefficient matrix  $\mathbf{C}^{(s)}$  is a symmetric matrix, while the cell bulk viscosity coefficient matrix  $\mathbf{C}^{(b)}$  is non-symmetric.

## C. Discussion

In this Discussion section, we review previously proposed implementations of cellular viscosity, with a particular focus on the questions of (1) rotation-invariance and (2) absence of friction on a fixed substrate.

### 1. Our model is invariant under rotational symmetry

Here we show that our model is invariant under a global rigid rotation represented by an orthogonal matrix  $\mathbf{R}$  satisfying  $\mathbf{R}^T \mathbf{R} = \mathbf{I}$  with  $\mathbf{I}$  an identity matrix. Positions and velocities transform as  $\mathbf{r}'_i = \mathbf{R} \mathbf{r}_i$ ,  $\mathbf{r}'_J = \mathbf{R} \mathbf{r}_J$  and  $\mathbf{v}'_i = \mathbf{R} \mathbf{v}_i$ ,  $\mathbf{v}'_J = \mathbf{R} \mathbf{v}_J$ . The unit vector  $\mathbf{t}_{i,j} = (\mathbf{r}_j - \mathbf{r}_i) / |\mathbf{r}_j - \mathbf{r}_i|$  then transforms as

$$\mathbf{t}'_{i,j} = \frac{\mathbf{r}'_j - \mathbf{r}'_i}{|\mathbf{r}'_j - \mathbf{r}'_i|} = \frac{\mathbf{R}(\mathbf{r}_j - \mathbf{r}_i)}{|\mathbf{R}(\mathbf{r}_j - \mathbf{r}_i)|} = \mathbf{R} \mathbf{t}_{i,j}, \quad (37)$$

where we have used the identity  $|\mathbf{R} \mathbf{a}| = |\mathbf{a}|$  for any vector  $\mathbf{a}$ . Hence

$$\mathbf{t}'_{i,j} \cdot (\mathbf{v}'_j - \mathbf{v}'_i) = (\mathbf{R} \mathbf{t}_{i,j}) \cdot (\mathbf{R}(\mathbf{v}_j - \mathbf{v}_i)) = \mathbf{t}_{i,j} \cdot (\mathbf{v}_j - \mathbf{v}_i), \quad (38)$$

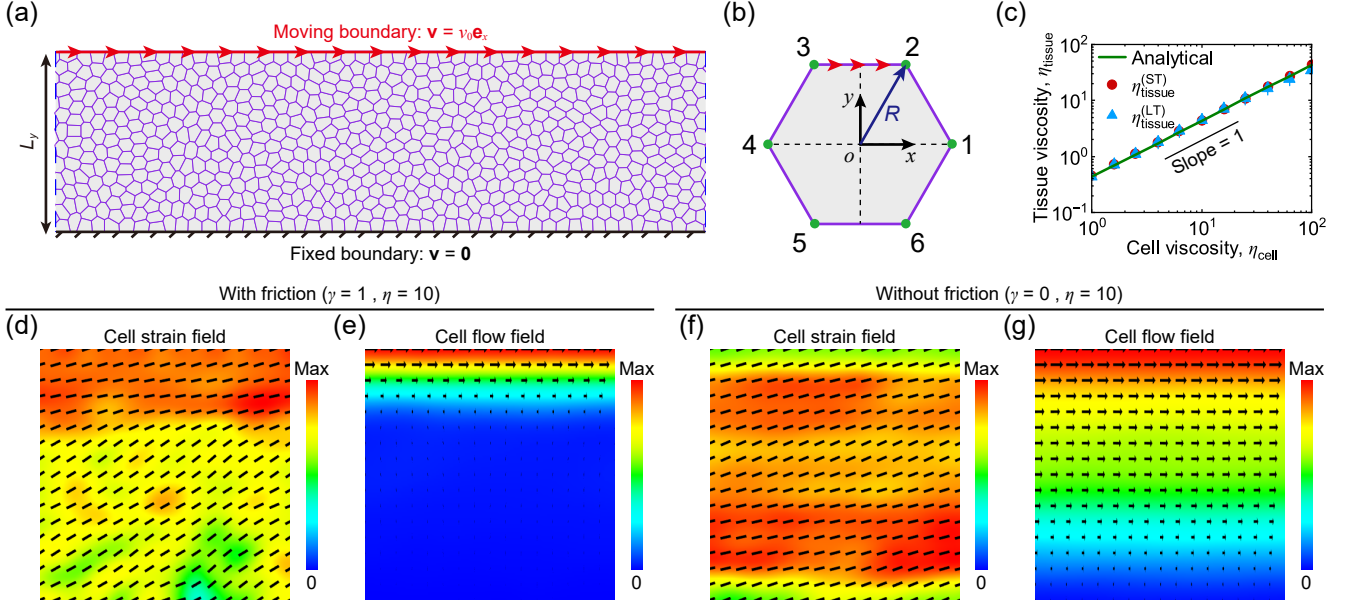


FIG. 3: Measuring the coarse-grained tissue viscosity. Here, we do not consider cell activities (i.e.,  $T_0 = 0$  and  $\beta = 0$ ). (a) Schematic of shearing a cell sheet within a slab geometry. The slab is assumed to be periodic along the  $x$ -axis and is of width  $L_y$  in the  $y$ -axis. Cell vertices adhered to the bottom border are fixed, i.e.  $\mathbf{v} = \mathbf{0}$ , while cell vertices adhered to the top border move at a specified velocity  $\mathbf{v} = v_0 \mathbf{e}_x$ . Thus, the global tissue shear strain rate is  $\dot{\gamma}_{xy} = v_0/L_y$ . (b) Theoretical analysis of a single hexagonal cell under a constant shear strain rate  $\dot{\gamma}_{xy}$ . (c) The short-time tissue viscosity  $\eta_{\text{tissue}}^{(\text{ST})}$  and the long-time tissue viscosity  $\eta_{\text{tissue}}^{(\text{LT})}$  as functions of cellular viscosity  $\eta = \eta_s = \eta_b$ . Comparison with the analytical result (Eq. (60)). (d-g) Comparisons of the cell deformation strain field (d, f) and the cell flow field (e, g) for the case with friction (d, e) and the case without friction (f, g), averaged over  $N_t = 100$  frames. In (d, f), the color code refers to the magnitude of the cell deformation tensor  $\epsilon_{\text{cell}}^{(\text{dev})}$  (the deviatoric part) and lines represent orientations. In (e, g), the color code indicates the magnitude of velocity, and the arrows represent the velocity vectors.

where we have used the identity  $(\mathbf{R}\mathbf{a}) \cdot (\mathbf{R}\mathbf{b}) = \mathbf{a} \cdot \mathbf{b}$  for orthogonal matrix  $\mathbf{R}$ . Therefore,

$$\begin{aligned} \Lambda_{i,j}^{(\text{viscous})'} &= \eta_{ij}^{(s)} \mathbf{t}'_{i,j} \cdot (\mathbf{v}'_j - \mathbf{v}'_i) = \eta_{ij}^{(s)} \mathbf{t}_{i,j} \cdot (\mathbf{v}_j - \mathbf{v}_i) \\ &= \Lambda_{i,j}^{(\text{viscous})}, \end{aligned} \quad (39)$$

showing that the viscous cell-cell interfacial tension defined in Eq. (3) is invariant under global rotations. Similarly, it is easy to prove that the viscous cell-bulk line tension defined in Eq. (5) is also invariant under global rotations.

The alternative formulation provided in previous studies (e.g., Refs. [34, 37]) is to assign a viscous force at vertex  $i$  of the form

$$\mathbf{F}_i^{(\text{visc,alt})} = -\eta \sum_{j \in S_i} (\dot{\mathbf{r}}_i - \dot{\mathbf{r}}_j), \quad (40)$$

with  $S_i$  the set of neighbours of  $i$ . This expression is *not* invariant under superposed rigid-body rotations (it violates material objectivity). Indeed, consider adding to the motion a solid-body rotation with angular velocity  $\mathbf{\Omega}$ ,  $\dot{\mathbf{r}}_k \rightarrow \dot{\mathbf{r}}'_k = \dot{\mathbf{r}}_k + \mathbf{\Omega} \times \mathbf{r}_k$ . The alternative viscous force Eq. (40) then transforms as

$$\mathbf{F}_i^{(\text{visc,alt})'} = \mathbf{F}_i^{(\text{visc,alt})} - \eta \sum_{j \in S_i} \mathbf{\Omega} \times (\mathbf{r}_i - \mathbf{r}_j). \quad (41)$$

The additional term to  $\mathbf{F}_i^{(\text{visc,alt})}$  is generically nonzero; in this model, a pure rigid-body rotation (no edge stretching) leads to dissipation. Yet a junctional viscosity should not penalize global rotations. In contrast, the junctional viscous law used in our model,  $\Lambda_{ij}^{(\text{visc})} \propto \mathbf{t}_{ij} \cdot (\dot{\mathbf{r}}_j - \dot{\mathbf{r}}_i)$ , is invariant under  $\dot{\mathbf{r}}_k \rightarrow \dot{\mathbf{r}}_k + \mathbf{\Omega} \times \mathbf{r}_k$  and therefore respects rotational symmetry.

In Ref. [35], dissipation is included by penalizing the rates of area and perimeter changes, resulting in a rotation-invariant scheme. However, in Ref. [35] the limit of vanishing cell-substrate friction (describing free-standing tissues) is not addressed: this is the subject of the next paragraph.

## 2. Implementation of the zero-friction case

Here, we address the limit of vanishing cell-substrate friction. This case is important since in several instances the friction between cells and their environment can be neglected compared to the cellular viscosity, e.g., in free-floating tissues [24, 26] and organoids [12, 38]. Based on the expressions of  $\mathbf{C}_{ij}^{(s)}$  and  $\mathbf{C}_{ij}^{(b)}$  (see Eqs. (28) and (29)),

we note that

$$\sum_{j=1}^{N_v} \mathbf{C}_{ij}^{(s)} = \mathbf{0} \quad , \quad \sum_{j=1}^{N_v} \mathbf{C}_{ij}^{(b)} = \mathbf{0}. \quad (42)$$

These two equations indicate that both the cell-cell interfacial viscosity coefficient matrix  $\mathbf{C}^{(s)}$  and the cell bulk viscosity coefficient matrix  $\mathbf{C}^{(b)}$  are singular. Therefore, in the limiting case of zero friction, i.e.,  $\gamma_i = \mathbf{0}$ , the total friction-viscosity coefficient matrix  $\mathbf{C}$  is singular. Physically, this is due to the unconstrained global translation and rotation of cells/vertices. To deal with this issue, one can assume a small friction, i.e.,  $\gamma/\eta \rightarrow 0$ . However, a super small friction may result in a large condition number of the friction-viscosity matrix  $\mathbf{C}$  (Fig. 2(a)), leading to numerical divergence; while a finite friction can not describe the case of zero friction well.

Here, we propose an alternative numerical simulation method. In the case of zero friction, there is no momentum exchange and no angular momentum exchange between the cell sheet and the environment. Furthermore, assuming that initially the total momentum and total angular momentum of the cell sheet system are both zero, we have the following constraints on  $\mathbf{v}_i$ :

$$\sum_{i=1}^{N_v} \mathbf{v}_i = \mathbf{0}, \quad (43)$$

and

$$\sum_{i=1}^{N_v} \mathbf{r}_i \times \mathbf{v}_i = \mathbf{0}. \quad (44)$$

These two constraints can be re-expressed as,

$$\mathbf{D} \cdot \mathbf{v} = \mathbf{0}, \quad (45)$$

where  $\mathbf{D}$  is a constraint matrix of size  $3 \times 2N_v$ . Introducing the Lagrange multiplier  $\boldsymbol{\lambda}$ , the motion equation (1) along with the constraint Eq. (45) can be together expressed as,

$$\mathbf{C}_{\text{ext}} \cdot \begin{pmatrix} \mathbf{v} \\ \boldsymbol{\lambda} \end{pmatrix} = \begin{pmatrix} \mathbf{F}^{(\text{t})} \\ \mathbf{0} \end{pmatrix}, \quad (46)$$

where

$$\mathbf{C}_{\text{ext}} = \begin{pmatrix} \mathbf{C} & \mathbf{D}^T \\ \mathbf{D} & \mathbf{0} \end{pmatrix} \quad (47)$$

is referred to as an extended viscosity coefficient matrix; in general,  $\mathbf{C}_{\text{ext}}$  is non-singular when  $\eta_J^{(b)} \neq 0$ . We check that the condition number of  $\mathbf{C}_{\text{ext}}$  (denoted  $\text{cond}(\mathbf{C}_{\text{ext}})$ ) is numerically feasible (Fig. 2(a, b)), thus ensuring its suitability for subsequent simulations. For example, for a cell sheet consisting of  $N_c = 1000$  cells,  $\text{cond}(\mathbf{C}_{\text{ext}}) \sim 10^6$ . We show an example of simulating an active cell sheet without friction in Fig. 2(c, d).

*Either substrate friction or bulk viscosity is needed.* The extended friction-viscous matrix defined in Eq. (47) is singular when  $\gamma = 0$  and  $\eta_J^{(b)} = 0$ . In this case, the only remaining source of dissipation in  $\mathbf{C}$  is the junctional viscosity  $\eta_{ij}^{(s)}$ , which penalizes changes in junctional lengths but does not generically oppose all possible vertex motions; in particular, there exist collective vertex velocity fields  $\mathbf{v}$  that preserve all edge lengths and, consistently with the constraint  $\mathbf{D} \cdot \mathbf{v} = 0$ , also preserve all cell areas. Such area- and length-preserving deformations correspond to floppy modes of the vertex network: they generate no viscous or frictional forces, so that one can find  $(\mathbf{v}, \boldsymbol{\lambda}) \neq \mathbf{0}$  satisfying

$$\mathbf{C}_{\text{ext}} \cdot \begin{pmatrix} \mathbf{v} \\ \boldsymbol{\lambda} \end{pmatrix} = \mathbf{0}. \quad (48)$$

In Fig. 2(e), we provide an example of the floppy mode in a cell layer consisting of  $N_c = 100$  cells in a square domain with periodic boundary conditions. To quantify the proportion of floppy modes, we define the fraction of floppy modes as  $f = 1 - \text{rank}(\mathbf{C}_{\text{ext}})/N_{\text{ext}}$  with  $N_{\text{ext}}$  being the size of the extended friction-viscous matrix  $\mathbf{C}_{\text{ext}}$ . We find that the fraction of floppy modes  $f$  increases with the number of cells  $N_c$ ; when  $N_c \rightarrow +\infty$ ,  $f \simeq 1/4$  (Fig. 2(f)).

The existence of these zero-dissipation modes implies that the extended friction-viscous matrix  $\mathbf{C}_{\text{ext}}$  is not invertible. Introducing either a finite substrate friction  $\gamma > 0$  or a finite bulk viscosity  $\eta_J^{(b)} > 0$  lifts these floppy modes by endowing rigid-body and other isometric motions with a finite dissipative cost, thereby regularizing  $\mathbf{C}_{\text{ext}}$  and restoring its invertibility.

*Boundary conditions can be redundant.* Note that if fixed boundaries or externally applied forces exist, implementing these boundary conditions via the Lagrange multiplier method (see Sec. III and IV) will also address the singular issue of the friction-viscosity matrix. In such cases, the boundary constraints Eqs. (43) and (44) are not necessary.

## D. Model simplification

In our present study, for simplicity, we assume a homogeneous and isotropic friction, i.e.,  $\gamma_i = \gamma \mathbf{I}$  with  $\gamma$  being a scalar friction coefficient. We also assume a homogeneous cell-cell interfacial viscosity and a homogeneous cell bulk viscosity across the whole tissue. Thus, we set  $\eta_{ij}^{(s)} = \eta_s$  for all cell-cell interfaces and  $\eta_J^{(b)} = \eta_b$  for all cells. In addition, we do not consider the tension fluctuations and thus set  $\zeta_{ij} = 0$  for all cell-cell interfaces  $ij$  and  $\zeta_{i,J} = 0$  for all cell-bulk segments  $iJ$  hereafter.

In our numerical simulations, if not stated otherwise, we set the following parameter values:  $K_A = 1$ ,  $A_0 = 1$ ,  $K_P = 0.02$ ,  $P_0 = 1$ , and  $\gamma = 1$ .

### III. CELL-CELL DISSIPATION AND COARSE-GRAINED TISSUE VISCOSITY

Here, we employ our viscous vertex model to relate the coarse-grained tissue viscosity  $\eta_{\text{tissue}}$  to the interfacial and bulk cell viscosities  $\eta_s$  and  $\eta_b$  in a purely passive vertex model, in which we set  $T_0 = 0$  and  $\beta = 0$ .

To do so, we consider a tissue in a slab geometry. We apply a fixed shear strain rate  $\dot{\gamma}_{xy}$  and measure the exerted stress.

#### A. Method

In this section, we consider a cell sheet adhered to a slab geometry of width  $L_y$ , as in Refs. [3, 48, 49], as shown in Fig. 3(a). We apply a shear strain rate  $\dot{\gamma}_{xy}$  to the cell sheet in the following way: (i) the cell vertices adhered to the bottom border is fixed, i.e.,  $\mathbf{v}_i = \mathbf{0}$  for all bottom vertices; (ii) the cell vertices adhered to the top border move at a prescribed velocity  $\mathbf{v}_i = v_0 \hat{\mathbf{x}}$  for all top vertices with  $v_0 = L_y \dot{\gamma}_{xy}$  and  $\hat{\mathbf{x}}$  a unit vector along the long axis of the slab (i.e.,  $x$  axis). Therefore, we have the following boundary conditions:

$$\mathbf{v}_i = \begin{cases} \mathbf{0} & \text{bottom boundary} \\ v_0 \hat{\mathbf{x}} & \text{top boundary} \end{cases} \quad (49)$$

which can be formulated in the matrix form as below:

$$\mathbf{D} \cdot \mathbf{v} = \mathbf{v}_b. \quad (50)$$

Introduce the Lagrange multiplier  $\boldsymbol{\lambda}$ , the vertices' velocity satisfy the following equation:

$$\begin{pmatrix} \mathbf{C} & \mathbf{D}^T \\ \mathbf{D} & \mathbf{0} \end{pmatrix} \cdot \begin{pmatrix} \mathbf{v} \\ \boldsymbol{\lambda} \end{pmatrix} = \begin{pmatrix} \mathbf{F}^{(t)} \\ \mathbf{v}_b \end{pmatrix} \quad (51)$$

#### B. Results

##### 1. Short-time tissue viscosity

Given the configuration of a cell sheet, i.e., the vertices' positions  $\{\mathbf{r}_i\}$  and the network topology, we can define the short-time tissue viscosity  $\eta_{\text{tissue}}^{(\text{ST})}$  as the following.

Solving Eq. (51), we obtain the velocity vector  $\mathbf{v}_i$  of each vertex  $i$ . Subsequently, we can calculate the viscous cell-cell interfacial tension  $\Lambda_{ij}^{(\text{viscous})}$  via Eq. (3) and the viscous cell-bulk line tension  $\Lambda_{i,J}^{(\text{viscous})}$  via Eq. (5). Then

we can calculate the tissue viscous shear stress as,

$$\sigma_{xy}^{(\text{viscous})} = \frac{\sum_{i,j} \Lambda_{ij}^{(\text{viscous})} l_{ij} t_{ij}^{(x)} t_{ij}^{(y)}}{\sum_J A_J} + \frac{\sum_J \sum_{i \in \text{cell } J} \Lambda_{i,J}^{(\text{viscous})} l_{i,J} t_{i,J}^{(x)} t_{i,J}^{(y)}}{\sum_J A_J}. \quad (52)$$

Finally, we can measure the coarse-grained short-time tissue viscosity as,

$$\eta_{\text{tissue}}^{(\text{ST})} = \frac{\sigma_{xy}^{(\text{viscous})}}{\dot{\gamma}_{xy}}. \quad (53)$$

From Eqs. (51)–(52), we know that the tissue viscosity  $\eta_{\text{tissue}}$  depends on only the viscous matrix  $\mathbf{C}$ , i.e., the cell-cell interfacial viscosity  $\eta_s$ , the cell bulk viscosity  $\eta_b$  as well as the geometry (vertices' positions) and topology (neighboring relationship) of the cell sheet. However, it should be noted that the geometry and topology of the cell sheet can be affected by cell mechanical properties and cell activity, which thus indirectly affect the tissue viscosity.

In addition, varying the shear strain rate  $\dot{\gamma}_{xy}$ , Eq. (51) leads to,

$$\begin{pmatrix} \mathbf{C} & \mathbf{D}^T \\ \mathbf{D} & \mathbf{0} \end{pmatrix} \cdot \begin{pmatrix} \delta \mathbf{v} \\ \delta \boldsymbol{\lambda} \end{pmatrix} = \begin{pmatrix} \mathbf{0} \\ \delta \mathbf{v}_b \end{pmatrix} \quad (54)$$

Thus, we have  $\delta \mathbf{v} \propto \delta \mathbf{v}_b \propto \delta \dot{\gamma}_{xy}$ , which leads to  $\delta \Lambda_{ij}^{(\text{viscous})} \propto \delta \dot{\gamma}_{xy}$  and  $\delta \Lambda_{i,J}^{(\text{viscous})} \propto \delta \dot{\gamma}_{xy}$ . Consequently,  $\delta \sigma_{xy}^{(\text{viscous})} \propto \delta \dot{\gamma}_{xy}$ . This suggests that the viscous shear stress  $\sigma_{xy}^{(\text{viscous})}$  is linearly related to the shear rate  $\dot{\gamma}_{xy}$ , as validated by our numerical simulations.

Our numerical simulations show that, in the absence of cellular activity, the short-time tissue viscosity  $\eta_{\text{tissue}}^{(\text{ST})}$  is linearly related to the cellular viscosity  $\eta = \eta_s = \eta_b$  (Fig. 3(c)). This is because, in the absence of cellular activity, the cellular viscosity does not affect the tissue morphology and topology.

To gain an analytical expression of the short-time tissue viscosity, here, we consider a hexagonal cell of radius  $R$ , as shown in Fig. 3(b). The coordinates of the  $k$ -th vertex read:  $x_k = R \cos[(k-1)\pi/3]$  and  $y_k = R \sin[(k-1)\pi/3]$  with  $k = 1, 2, \dots, 6$ . Now we fix the fifth and sixth vertices and apply a uniform shear strain rate  $\dot{\gamma}_{xy}$  to the hexagonal cell. The velocity of each vertex reads,

$$\begin{aligned} \mathbf{v}_1 = \mathbf{v}_4 &= \frac{\sqrt{3}}{2} R \dot{\gamma}_{xy} \hat{\mathbf{x}}, \\ \mathbf{v}_2 = \mathbf{v}_3 &= \sqrt{3} R \dot{\gamma}_{xy} \hat{\mathbf{x}}, \\ \mathbf{v}_5 = \mathbf{v}_6 &= \mathbf{0}. \end{aligned} \quad (55)$$

Thus, we can calculate the viscous cell-cell interfacial tension as,

$$\begin{aligned}\Lambda_{12}^{(\text{viscous})} &= \Lambda_{45}^{(\text{viscous})} = -\frac{\sqrt{3}}{4}\eta_s R \dot{\gamma}_{xy}, \\ \Lambda_{34}^{(\text{viscous})} &= \Lambda_{61}^{(\text{viscous})} = \frac{\sqrt{3}}{4}\eta_s R \dot{\gamma}_{xy}, \\ \Lambda_{23}^{(\text{viscous})} &= \Lambda_{56}^{(\text{viscous})} = 0.\end{aligned}\quad (56)$$

and the viscous cell-bulk line tension as,

$$\begin{aligned}\Lambda_{1,J}^{(\text{viscous})} &= \Lambda_{4,J}^{(\text{viscous})} = 0, \\ \Lambda_{2,J}^{(\text{viscous})} &= \Lambda_{5,J}^{(\text{viscous})} = \frac{\sqrt{3}}{4}\eta_b R \dot{\gamma}_{xy}, \\ \Lambda_{3,J}^{(\text{viscous})} &= \Lambda_{6,J}^{(\text{viscous})} = -\frac{\sqrt{3}}{4}\eta_b R \dot{\gamma}_{xy}.\end{aligned}\quad (57)$$

Consequently, the total viscous shear stress reads,

$$\sigma_{xy}^{(\text{viscous})} = \frac{1}{4\sqrt{3}}\eta_s \dot{\gamma}_{xy} + \frac{1}{2\sqrt{3}}\eta_b \dot{\gamma}_{xy}. \quad (58)$$

Finally, we obtain the short-time tissue viscosity as,

$$\eta_{\text{tissue}}^{(\text{ST})} = \frac{\sigma_{xy}^{(\text{viscous})}}{\dot{\gamma}_{xy}} = \frac{1}{4\sqrt{3}}\eta_s + \frac{1}{2\sqrt{3}}\eta_b. \quad (59)$$

In particular, when  $\eta_s = \eta_b = \eta$ , we obtain a simple relation between the short-time tissue viscosity and the cellular viscosity as,

$$\eta_{\text{tissue}}^{(\text{ST})} = \frac{\sqrt{3}}{4}\eta. \quad (60)$$

This analytical expression agrees well with our numerical calculations (Fig. 3(c)).

## 2. Long-time tissue viscosity

The calculation of the short-time tissue viscosity does not include cell-cell rearrangement, and can fail to account for the long-time tissue response to applied shear strain/stress.

Here, we apply a constant and sustained shear strain rate  $\dot{\gamma}_{xy}$  to the tissue. We allow cell motions and cell-cell rearrangement and monitor the evolution of the tissue viscous stress  $\sigma_{xy}^{(\text{viscous})}(t)$  under the sustained shear strain rate  $\dot{\gamma}_{xy}$ . This allows us to evaluate the long-time tissue viscosity as:

$$\eta_{\text{tissue}}^{(\text{LT})} = \frac{\langle \sigma_{xy}^{(\text{viscous})}(t) \rangle}{\dot{\gamma}_{xy}}, \quad (61)$$

where  $\langle \cdot \rangle$  is an average over time.

When friction dominates, we observe localized shear banding near the moving boundary (Fig. 3(d,e)).

When friction is negligible, i.e.,  $\gamma = 0$ , as expected, shear banding vanishes, and the shear flow field is consistent with the one observed in a Newtonian fluid, see Fig. 3(f,g). In this regime, we find that the long-time tissue viscosity  $\eta_{\text{tissue}}^{(\text{LT})}$  is close to (but lower than) the short-time tissue viscosity  $\eta_{\text{tissue}}^{(\text{ST})}$ , especially at small cellular viscosity. At larger cellular viscosities (larger  $\eta_s$  and larger  $\eta_b$ ), the long-time tissue viscosity  $\eta_{\text{tissue}}^{(\text{LT})}$  becomes distinguishable from the short-time tissue viscosity  $\eta_{\text{tissue}}^{(\text{ST})}$ . This is because at high cellular viscosity, cell deformation can not be relaxed within the applied shear stress time scale.

## C. Discussion

In the framework of Nestor-Bergmann *et al.* [35], the resulting cell stress tensor contains viscous contributions proportional to the cell area expansion rate  $\dot{A}_J$  (associated with a bulk viscosity  $\mu_b$ ) and the perimeter elongation rate  $\dot{P}_J$  (associated with a cortical viscosity  $\mu_c$ ). The coarse-grained tissue shear stress is obtained by summing these over all cells; in the linear regime, the effective shear viscosity thus appears as a geometric prefactor multiplying a strictly linear combination of the microscopic viscosities  $\mu_b$  and  $\mu_c$  [35].

In Ref. [50], an oscillatory shear was applied to a vertex model in the presence of substrate friction. Ref. [51] developed a normal-mode analysis of the vertex model with both external (cell-substrate) and internal (cell-cell) dissipation. In their formulation, the overdamped dynamics is written as  $\hat{\mathbf{C}} \cdot \dot{\mathbf{r}} = -\hat{\mathbf{H}} \cdot \delta\mathbf{r}$ , where  $\hat{\mathbf{H}}$  is the Hessian matrix and the generalized friction matrix  $\hat{\mathbf{C}}$  is a linear combination of microscopic friction coefficients associated with each dissipation mechanism. Each normal mode then behaves as a viscoelastic element combining a standard linear solid (elastic) contribution with a Jeffreys-type viscous element; the loss moduli are linear in the entries of  $\hat{\mathbf{C}}$ , leading to the conclusion that the macroscopic viscosities extracted from the shear moduli depend linearly on the microscopic friction parameters, as the short-time tissue viscosity in our study. Yet, cell rearrangements, which can relax stresses, were not considered therein [51].

In other rheological extensions of the vertex model, including Refs. [52, 53], with all overdamped formulations, a long-time macroscopic tissue viscosity is estimated, but not expressed in terms of the interfacial viscosity.

## IV. CELL-CELL DISSIPATION AND ACTIVITY: LARGE-SCALE TISSUE FLOWS

### A. Drag on a cell or a cell cluster

To better illustrate the effect of cellular viscosity, here, we perform numerical simulations of pulling a cell within

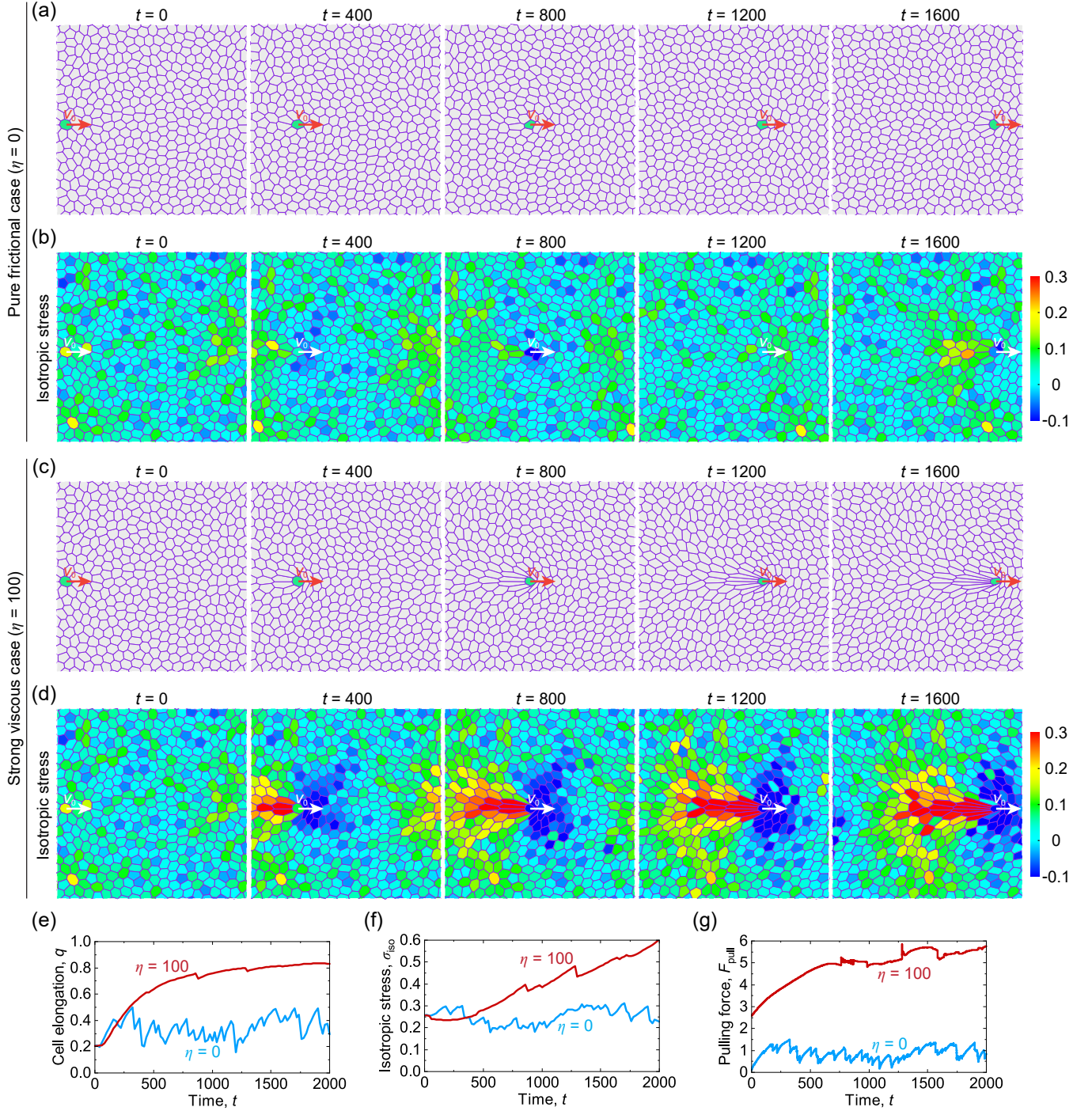


FIG. 4: Numerical simulation of pulling a cell within a passive cell sheet with a constant pulling velocity  $v_0$ . Here, we do not consider cellular activities and assume  $\eta_s = \eta_b = \eta$ . Comparison of (a, b) the pure frictional case ( $\eta = 0$ ) and (c, d) the strong viscous case ( $\eta = 100$ ). (a, c) Evolution of cell morphologies. Here, we mark the cell under pulling in green. (b, d) Evolution of the isotropic stress within cells. (e) Comparison of the average cell elongation (of neighboring cells of the cell under pulling) for the pure frictional case and the strong viscous case. (f) Comparison of the average isotropic stress (of neighboring cells of the cell under pulling) for the pure frictional case and the strong viscous case. (g) Comparison of the pulling force for the pure frictional case and the strong viscous case. Parameters:  $T_0 = 0$ ,  $\beta = 0$ ,  $v_0 = 0.01$ , and  $\gamma = 1$ .

a passive epithelial cell sheet. We first provide details on the method before discussing our results.

### 1. Method

Let us first consider the case where a sustaining drag is applied to a cell or a cell cluster. For example, here,

we assume that a sustaining drag is applied to the cell  $J$  with a constant velocity  $\mathbf{v}_0$ . We have the following boundary condition:

$$\frac{1}{n_J} \sum_{i \in \text{cell } J} \mathbf{v}_i = \mathbf{v}_0, \quad (62)$$

that is,

$$\mathbf{D} \cdot \mathbf{v} = \mathbf{v}_0, \quad (63)$$

where  $\mathbf{D} = (\mathbf{D}_i)_{2 \times 2N_v}$  is the constraint matrix with  $\mathbf{D}_i$  being

$$\mathbf{D}_i = \begin{cases} \frac{1}{n_J} \mathbf{I} & , \quad i \in \text{cell } J \\ \mathbf{0} & , \quad \text{otherwise} \end{cases} \quad (64)$$

Introducing the Lagrange multiplier  $\boldsymbol{\lambda} = (\lambda_1, \lambda_2)^T$ , the motion equation (1) along with the boundary constraint Eq. (63) can be together expressed as,

$$\begin{pmatrix} \mathbf{C} & \mathbf{D}^T \\ \mathbf{D} & \mathbf{0} \end{pmatrix} \cdot \begin{pmatrix} \mathbf{v} \\ \boldsymbol{\lambda} \end{pmatrix} = \begin{pmatrix} \mathbf{F}^{(t)} \\ \mathbf{v}_0 \end{pmatrix}, \quad (65)$$

which is equivalent to

$$\begin{cases} \mathbf{C} \cdot \mathbf{v} = \mathbf{F}^{(t)} - \mathbf{D}^T \cdot \boldsymbol{\lambda} \\ \mathbf{D} \cdot \mathbf{v} = \mathbf{v}_0 \end{cases} \quad (66)$$

Therefore, the term  $-\mathbf{D}^T \cdot \boldsymbol{\lambda}$  corresponds to the reaction forces induced by the boundary constraint – pulling force here. The total pulling force can be calculated by,

$$\mathbf{F}_{\text{pull}} = \sum_{i \in \text{cell } J} (-\mathbf{D}_i^T \cdot \boldsymbol{\lambda}) = -\boldsymbol{\lambda}. \quad (67)$$

## 2. Results

We perform numerical simulations of pulling a cell within a passive epithelial cell sheet ( $T_0 = 0$  and  $\beta = 0$ ) with a constant drag velocity  $v_0 = 0.01$ . Here, we set  $\gamma = 1$  and  $\eta_s = \eta_b = \eta$ . We compare two limiting cases: (1) pure frictional case ( $\eta = 0$ ); (2) strong viscous case ( $\eta = 100$ ).

We present the typical cell morphologies and the isotropic stress field for these two cases in Fig. 4(a-d). It shows that in the pure frictional case ( $\eta = 0$ ), the cell deformation and the cell stress are relaxed (Fig. 4(a, e, f)). In contrast, in the strong viscous case ( $\eta = 100$ ), cells around the cell under pulling exhibit large deformations (Fig. 4(c, e)), leading to large stresses (Fig. 4(c, f)). We also find that the total pulling force  $F_{\text{pull}}$  for the strong viscous case is much larger than that for the pure frictional case (Fig. 4(g)), because a larger pulling force is needed to overcome the large cell deformations.

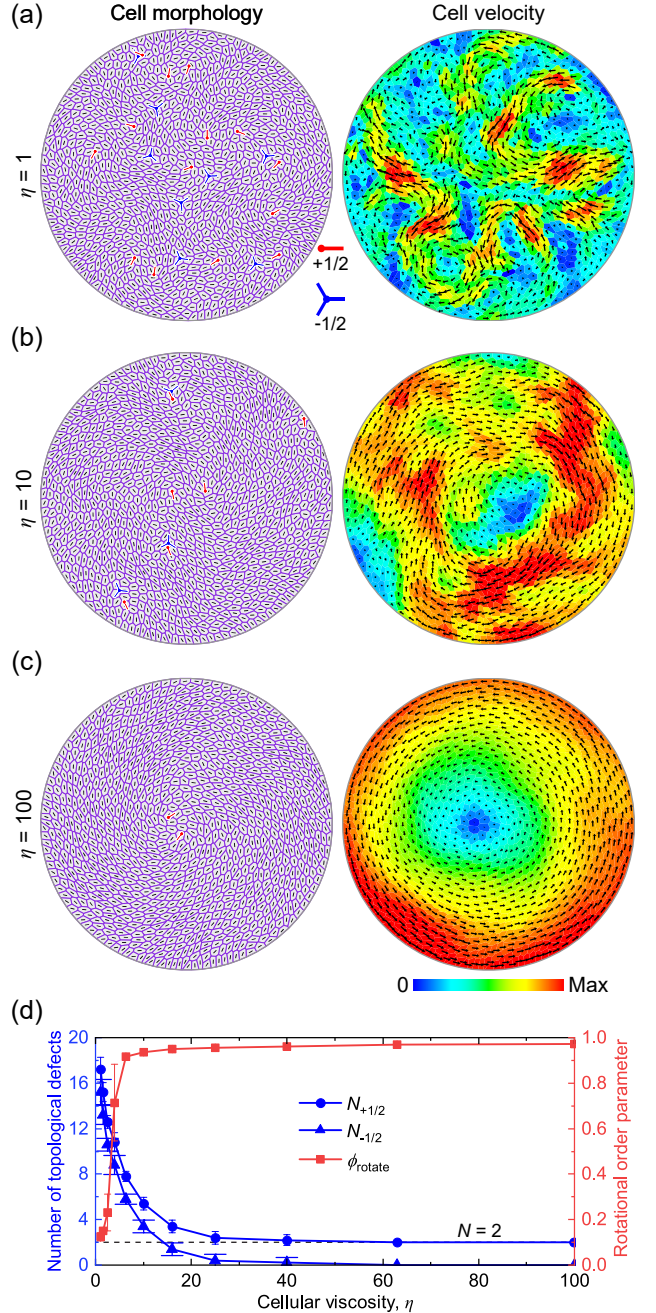


FIG. 5: Numerical simulation of viscous, polar, active tissue flows in a circular domain. (a-c) The cell morphology (left) and the cell velocity field (right) at various levels of cell viscosity  $\eta_b = \eta_b = \eta$ : (a)  $\eta = 1$ ; (b)  $\eta = 10$ ; (c)  $\eta = 100$ . The black lines represent cell orientation and the red (resp. blue) symbols indicate the locations and orientations of  $+1/2$  (resp.  $-1/2$ ) topological defects, extracted using the scheme proposed in Ref. [21]. The arrows represent cell velocity vectors, and the color code refers to the cell velocity magnitude. (d) The number of topological defects and the rotational order parameter as functions of the cellular viscosity  $\eta$ , averaged over  $n = 5$  independent simulations. Parameters:  $T_0 = 0.05$ ,  $D_r = 0.05$ ,  $\mu_{\text{LA}} = 0.05$ , and  $\mu_{\text{CIL}} = 1$ .

## B. Polar active traction

### 1. Method

Here, we consider the case of polar active traction forces, setting active stress to zero ( $\beta = 0$ ). The polar active traction force of a cell is usually modeled as

$$\mathbf{F}_J^{(\text{active})} = T_0 \mathbf{p}_J, \quad (68)$$

where  $T_0$  denotes the typical magnitude of the traction force and  $\mathbf{p}_J$  is the direction vector (referred to as the polarization vector) [19, 40–42, 54], as shown in Fig. 1(e). The active force at each vertex, induced by the active traction forces of the surrounding cells, is then approximated by averaging the active traction forces around the vertex, i.e.,  $\mathbf{F}_i^{(\text{active})} = \langle \mathbf{F}_J^{(\text{active})} \rangle_{J \in C_i}$ , where  $C_i$  is the set of cells neighboring vertex  $i$ .

The polarization vector  $\mathbf{p}_J$  evolves under the combined influence of intercellular social interactions (e.g., local alignment (LA) and contact inhibition of locomotion (CIL)) and diffusive noise [19, 41, 42]. Following Ref. [19], we express the dynamic equation of  $\mathbf{p}_J$  as

$$\begin{aligned} \frac{d\mathbf{p}_J}{dt} = & \mu_{\text{LA}} \frac{1}{n_J} \sum_{K \in \text{neighbor}} \sin(\theta_K^{(\text{vel})} - \theta_J) \\ & + \mu_{\text{CIL}} \frac{1}{n_J} \sum_{K \in \text{neighbor}} \sin(\alpha_{J,K} - \theta_J) \\ & + \sqrt{2D_r} \xi_J^R(t), \end{aligned} \quad (69)$$

where  $\mu_{\text{LA}}$  and  $\mu_{\text{CIL}}$  represent the intensities of LA and CIL, respectively;  $D_r$  refers to a rotational diffusion coefficient, and  $\xi_J^R(t)$  are independent unit-variance Gaussian white noises. In detail, the first term in Eq. (69) accounts for the tendency of a cell to follow the motion direction of its neighbors (equivalent to a Vicsek-type, local alignment interaction), where  $\theta_K^{(\text{vel})} = \arg(\mathbf{v}_K)$  is the immediate motion direction of cell  $K$  and the summation  $\sum_{K \in \text{neighbor}}$  is over all contacting neighbor cells of the  $J$ -th cell. The second term in Eq. (69) describes the tendency of a cell to move away from its neighbors upon contact, i.e., a repulsion interaction, where  $\alpha_{J,K} = \arg(\mathbf{r}_J - \mathbf{r}_K)$  refers to the argument of the direction pointing from cell  $K$  to cell  $J$ . The third term in Eq. (69) accounts for the random rotational diffusion of cell polarization vectors.

We consider a disk-like geometry [19, 36, 40] with boundary vertices allowed to slide freely along the boundary. Thus, the boundary condition reads:  $\mathbf{v}_i \cdot \mathbf{n}_i = 0$  for all boundary vertices, where  $\mathbf{n}_i$  represents the unit vector normal to the boundary at the vertex  $i$ . Introducing the Lagrange multiplier  $\boldsymbol{\lambda} = (\lambda_1, \lambda_2)^T$ , the overall motion equation can be expressed as in Eq. (51) with  $\mathbf{v}_b = 0$  here.

## 2. Results

We perform numerical simulations in a circular domain with a diameter much larger than the intrinsic swirl size of the cell sheet at the vanishing viscosity limit [19]. Thus, at low cellular viscosity  $\eta = \eta_s = \eta_b$ , we observe turbulent-like flows with many motile topological defects, which are singular points in the cell orientation pattern (Fig. 5(a)). Increasing cellular viscosity results in enhanced spatial correlation in cell orientation (marked by a decrease in the number of topological defects) and an enlarged swirl size (Fig. 5(b)). At larger cellular viscosity, we observe a global disk-like rotation mode, accompanied by two rotating  $+1/2$  topological defects, located in the center region of the circular domain (Fig. 5(c)). The mode transition is further verified by quantifying the number of topological defects  $N_{\pm 1/2}$  and the rotational order parameter  $\phi_{\text{rotate}} = \langle (1/N_c) \sum_J \hat{\mathbf{v}}_J \cdot \mathbf{e}_{\varphi,J} \rangle_t$  with  $\hat{\mathbf{v}}_J = \mathbf{v}_J / |\mathbf{v}_J|$  and  $\mathbf{e}_{\varphi,J}$  the local circumferential direction at cell  $J$ .

## C. Nematic active stresses

Here, we focus on a nematic active vertex model and turn off the polar active traction force ( $T_0 = 0$ ).

### 1. Method

Here, we consider the case of the apolar cellular active stress. In many cases, the apolar cellular active stress is anisotropic and depends on the cell shape [55–57]. In the linear order, the cell-shape-dependent active stress can be modeled as

$$\boldsymbol{\sigma}_J^{(\text{active})} = -\beta \mathbf{Q}_J, \quad (70)$$

with  $\beta$  being an activity parameter and  $\mathbf{Q}_J$  the cell shape tensor [21, 36, 37, 45], as shown in Fig. 1(f). The sign of  $\beta$  quantifies whether a cell actively pulls or pushes its neighbors (Fig. 1(f)): when  $\beta > 0$ , a cell actively pushes its neighbors along its shape elongation direction; otherwise, a cell actively pulls its neighbors along its shape elongation direction.

There are several different ways to define the cell shape tensor, including the cell edge-based scheme, the cell vertex-based scheme, and the cell area-based scheme [21]. These different ways lead to similar cell shape and pattern transitions [21]. Here, using a cell edge-based scheme, we define the cell shape tensor as in Ref. [21],

$$\mathbf{Q}_J = \frac{1}{P_J} \sum_{k \in \text{cell } J} l_k \mathbf{t}_k \otimes \mathbf{t}_k - \frac{1}{2} \mathbf{I}, \quad (71)$$

where  $l_k = |\mathbf{r}_{k+1} - \mathbf{r}_k|$  and  $\mathbf{t}_k = (\mathbf{r}_{k+1} - \mathbf{r}_k) / l_k$  are the length and direction of the  $k$ -th edge (pointing from vertex  $k$  to vertex  $k+1$ ) of the  $J$ -th cell. The cell shape

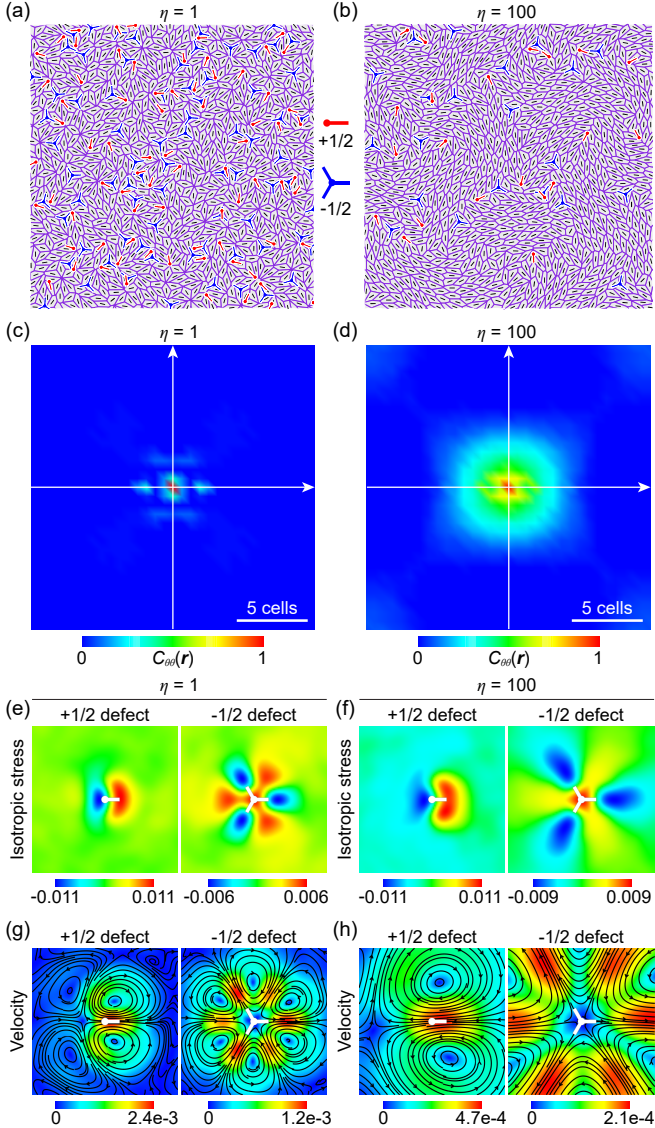


FIG. 6: Numerical simulation of a viscous, active nematic vertex model in a square domain with periodic boundary conditions. Here, we set  $\eta_s = \eta_b = \eta$ . (a, b) Typical cell morphologies at different cell viscosities: (a)  $\eta = 1$ ; (b)  $\eta = 100$ . The black lines indicate cell orientations; the red (resp. blue) symbols represent  $+1/2$  (resp.  $-1/2$ ) topological defects, extracted using the scheme proposed in Ref. [21]. (c, d) The spatial correlation map  $C_{\theta\theta}(\mathbf{r})$  of cell shape orientation at different cell viscosities: (c)  $\eta = 1$ ; (d)  $\eta = 100$ . Scale bar = 5 cell length. The spatial correlation function is defined as  $C_{\theta\theta}(\mathbf{r}) = \langle \cos 2(\theta_J - \theta_K) \rangle$ , where  $\langle \cdot \rangle$  averages over all cell pairs ( $J, K$ ) satisfying  $|(\mathbf{r}_J - \mathbf{r}_K) - \mathbf{r}| < \Delta r$ . (e, f) The average isotropic stress and (g, h) the average flow field near topological defects at different cellular viscosities: (e, g)  $\eta = 1$ ; (f, h)  $\eta = 100$ . In (e, f), the color code refers to the local stress fluctuation  $\sigma_{\text{iso}} - \langle \sigma_{\text{iso}} \rangle$ . In (g, h), the color code refers to the velocity magnitude, and the black lines with arrows represent flow directions. The number of defects for average: (e, g)  $n_{\pm 1/2} = 135805$ ; (f, h)  $n_{\pm 1/2} = 53307$ . Domain size  $L = 16$ . Parameters:  $T_0 = 0$  and  $\beta = 0.4$ .

tensor  $\mathbf{Q}_J$  is traceless and quantifies the elongation (corresponding to the positive eigenvalue of  $\mathbf{Q}_J$ ) and orientation (corresponding to the eigenvector associated with the positive eigenvalue of  $\mathbf{Q}_J$ ) of the  $J$ -th cell.

The force at each vertex induced by the active stress  $\sigma_J^{(\text{active})}$  can be calculated by the Cauchy stress formula [21, 58, 59], that is, by projecting the active stress of a cell to its edges.

## 2. Results

Here, we consider a square domain with periodic boundary conditions. We find that at low cellular viscosity, strong active stresses lead to elongated cell shape and multicellular rosettes, accompanied by a high density of topological defects, as shown in Fig. 6(a). This is consistent with our previous study of an active nematic vertex model at a vanishing cell viscosity limit [21]. At high cellular viscosity, we observe spatially long-range correlated cell orientations and well-defined topological defects (Fig. 6(b-d)); these features are close to those observed in experiments [36, 60–63].

We further examine the isotropic stress field and the flow field near topological defects, averaged over more than 50000 topological defects (see Ref. [21] for the average scheme), as shown in Fig. 6(e-h). These fields are consistent with active nematic gel theory and reported experiments [36, 60, 62, 63]. As expected, a stronger cellular viscosity results in stress and flow patterns of longer correlation length.

## D. Discussion

In Ref. [36], the emergence of multicellular topological defects was obtained in the presence of nematic alignment coupling between neighbouring cells. Here, we show that viscosity alone is sufficient to obtain large-scale topological defects.

We obtain similar spontaneous flows upon considering a slab geometry and active stresses with no-slip boundary conditions as in Ref. [37]. In Ref. [35], active traction and stresses are not considered and are formulated for substrates that effectively provide a fixed reference frame.

## V. CONCLUSION

Our work introduces a viscous extension of the vertex model in which dissipation arises from two microscopic sources: junctional viscosity along cell-cell interfaces and bulk viscous drag between vertices and cell centers. Both contributions are formulated in a rotationally invariant way, depending only on relative velocities projected along cell edges and vertex-cell segments, and assembled into a friction-viscosity matrix that governs the overdamped dynamics. A Lagrange multiplier framework is used to

impose kinematic constraints, which regularizes the dynamics in the zero-friction limit and provides a unified way to implement fixed, sliding, and driven boundaries, as well as global momentum and angular-momentum conservation.

On this basis, a constrained slab-shear protocol is proposed to extract a coarse-grained tissue viscosity directly from vertex velocities and line tensions. An analytical calculation for a single hexagonal cell and numerical simulations of disordered packings show that the short-time tissue viscosity scales linearly with both junctional and bulk cellular viscosities, whereas sustained shear in frictionless systems allows for a long-time viscosity to be defined in the presence of cell rearrangements. The same viscous vertex model is then applied to active polar and nematic tissues, where cellular viscosity is shown to elongate and align cells, reduce defect density, and reorganize active flows under confinement, driving a crossover from defect-rich active turbulence to coherent motion. Because the formulation remains well-posed at vanishing substrate friction and interfaces naturally with active nematic descriptions, it offers a useful bridge be-

tween cell-resolved simulations and continuum theories of free-standing tissues and organoids, and provides a framework for quantitatively interpreting future rheological measurements in living epithelia.

## Acknowledgments

S.Z.L. acknowledges support from the National Natural Science Foundation of China (Grant No. 12502367), Research Center for Magnetoelectric Physics of Guangdong Province (Grants 2024B0303390001), and Guangdong Provincial Key Laboratory of Magnetoelectric Physics and Devices (Grants 2022B1212010008). J.-F.R. acknowledges support from France 2030, the French Government program managed by the French National Research Agency (ANR-16-CONV-0001) from Excellence Initiative of Aix-Marseille University - A\*MIDEX. J.-F.R. and S.-Z.L. thank M. Merkel for interesting discussions. J.-F.R. and S.T. thank Nishchhal Verma for helpful discussions.

---

[1] G. Forgacs, R. A. Foty, Y. Shafrir, and M. S. Steinberg, *Biophysical Journal* **74**, 2227 (1998).

[2] S. Tlili, M. Durande, C. Gay, B. Ladoux, F. Graner, and H. Delanoë-Ayari, *Physical Review Letters* **125**, 088102 (2020).

[3] C. Fu, F. Dilasser, S.-Z. Lin, M. Karnat, A. Arora, H. Rajendiran, H. T. Ong, N. M. H. Brenda, S. W. Phow, T. Hirashima, M. Sheetz, J.-F. Rupprecht, S. Tlili, and V. Viasnoff, *Proceedings of the National Academy of Sciences of the United States of America* **121**, e2405560121 (2024).

[4] N. Khalilgharibi, J. Fouchard, N. Asadipour, R. Barrientos, M. Duda, A. Bonfanti, A. Yonis, A. Harris, P. Mosaffa, Y. Fujita, *et al.*, *Nature Physics* **15**, 839 (2019).

[5] A. Arora, M. S. Rizvi, G. Grenci, F. Dilasser, C. Fu, M. Ganguly, S. Vaishnavi, K. Paramasivam, S. Budnar, I. Noordstra, *et al.*, *Nature Materials* **24**, 1126–1136 (2025).

[6] M. Karnat, G. H. Narayana, S. K. Peneti, V. Guglielotti, Q. S. Rahaman, S. Jain, B. Ladoux, S.-Z. Lin, S. Tlili, R.-M. Mège, and J.-F. Rupprecht, *Noninvasive rheological inference from stable flows in confined tissues* (2025), arXiv:2511.20155 [cond-mat.soft].

[7] K. Nishizawa, S.-Z. Lin, C. Chardès, J.-F. Rupprecht, and P.-F. Lenne, *Proceedings of the National Academy of Sciences of the United States of America* **120**, e2212389120 (2023).

[8] X.-Q. Feng, B. Li, S.-Z. Lin, M.-Y. Wang, X.-D. Chen, H.-X. Zhang, and W. Fang, *Acta Mechanica Sinica* **41**, 625315 (2025).

[9] B. Cheng, M. Li, M. Lin, H. Guo, and F. Xu, *Nature Reviews Physics* , 1 (2025).

[10] R. Clément, B. Dehapiot, C. Collinet, T. Lecuit, and P.-F. Lenne, *Current Biology* **27**, 3132 (2017).

[11] H. Sun, Y. Yang, and H. Jiang, *Biophysical Journal* **125**, 152 (2026).

[12] S. Gsell, S. Tlili, M. Merkel, and P.-F. Lenne, *Nature Physics* , 1 (2025).

[13] J. Prost, F. Jülicher, and J.-F. Joanny, *Nature Physics* **11**, 111 (2015).

[14] M. R. Shaebani, A. Wysocki, R. G. Winkler, G. Gompper, and H. Rieger, *Nature Reviews Physics* **2**, 181 (2020).

[15] S. Shankar, A. Souslov, M. J. Bowick, M. C. Marchetti, and V. Vitelli, *Nature Reviews Physics* **4**, 380 (2022).

[16] A. G. Fletcher, M. Osterfield, R. E. Baker, and S. Y. Shvartsman, *Biophysical Journal* **106**, 2291 (2014).

[17] D. Bi, J. H. Lopez, J. M. Schwarz, and M. L. Manning, *Nature Physics* **11**, 1074 (2015).

[18] S.-Z. Lin, B. Li, and X.-Q. Feng, *Acta Mechanica Sinica* **33**, 250 (2017).

[19] S.-Z. Lin, S. Ye, G.-K. Xu, B. Li, and X.-Q. Feng, *Biophysical Journal* **115**, 1826 (2018).

[20] S.-Z. Lin, Y. Li, J. Ji, B. Li, and X.-Q. Feng, *Soft Matter* **16**, 2941 (2020).

[21] S.-Z. Lin, M. Merkel, and J.-F. Rupprecht, *Physical Review Letters* **130**, 058202 (2023).

[22] Y. Chen, Q. Gao, J. Li, F. Mao, R. Tang, and H. Jiang, *Physical Review Letters* **128**, 018101 (2022).

[23] S. Alt, P. Ganguly, and G. Salbreux, *Philosophical Transactions of the Royal Society B: Biological Sciences* **372**, 20150520 (2017).

[24] A. R. Harris, L. Peter, J. Bellis, B. Baum, A. J. Kabla, and G. T. Charras, *Proceedings of the National Academy of Sciences of the United States of America* **109**, 16449 (2012).

[25] S. Armon, M. S. Bull, A. Aranda-Diaz, and M. Prakash, *Proceedings of the National Academy of Sciences of the United States of America* **115**, 1 (2018).

[26] J. Duque, A. Bonfanti, J. Fouchard, L. Baldauf, S. R. Azenha, E. Ferber, A. Harris, E. H. Barriga, A. J. Kabla, and G. Charras, *Nature Materials* **23**, 1563 (2024).

[27] A. D'Angelo, K. Dierkes, C. Carolis, G. Salbreux, and J. Solon, *Current Biology* **29**, 1564 (2019).

[28] K. Doubrovinski, M. Swan, O. Polyakov, and E. F. Wieschaus, *Proceedings of the National Academy of Sciences of the United States of America* **114**, 1051 (2017).

[29] H. Turlier, B. Audoly, J. Prost, and J.-F. Joanny, *Biophysical Journal* **106**, 114 (2014).

[30] J.-F. Rupprecht, A. S. Vishen, G. V. Shivashankar, M. Rao, and J. Prost, *Physical Review Letters* **120**, 098001 (2018).

[31] P.-F. Lenne, J.-F. Rupprecht, and V. Viasnoff, *Developmental Cell* **56**, 202 (2021).

[32] J. Yang and G. W. Brodland, *Annals of Biomedical Engineering* **37**, 1019 (2009).

[33] G. W. Brodland, J. Yang, and J. Sweny, *HFSP Journal* **3**, 273 (2009).

[34] S. Okuda, Y. Inoue, M. Eiraku, T. Adachi, and Y. Sasai, *Biomechanics and Modeling in Mechanobiology* **14**, 413 (2015).

[35] A. Nestor-Bergmann, E. Johns, S. Woolner, and O. E. Jensen, *Physical Review E* **97**, 052409 (2018).

[36] S. Sonam, L. Balasubramaniam, S.-Z. Lin, Y. M. Y. Ivan, I. Pi-Jaumà, C. Jebane, M. Karnat, Y. Toyama, P. Marcq, J. Prost, R.-M. Mège, J.-F. Rupprecht, and B. Ladoux, *Nature Physics* **19**, 132 (2023).

[37] J. Rozman, K. Chaithanya, J. M. Yeomans, and R. Sknepnek, *Nature Communications* **16**, 1 (2025).

[38] Z.-Y. Li, Y.-P. Chen, H.-Y. Liu, and B. Li, *Physical Review Letters* **132**, 138401 (2024).

[39] S.-Z. Lin, B. Li, G. Lan, and X.-Q. Feng, *Proceedings of the National Academy of Sciences* **114**, 8157 (2017).

[40] B. Li and S. X. Sun, *Biophysical Journal* **107**, 1532 (2014).

[41] D. Bi, X. Yang, M. C. Marchetti, and M. L. Manning, *Physical Review X* **6**, 021011 (2016).

[42] D. L. Barton, S. Henkes, C. J. Weijer, and R. Sknepnek, *PLoS Computational Biology* **13** (2017).

[43] X. Chen, Y. Li, M. Guo, B. Xu, Y. Ma, H. Zhu, and X.-Q. Feng, *Proceedings of the National Academy of Sciences of the United States of America* **120**, e2306512120 (2023).

[44] Q. Wang, S. He, and B. Ji, *Journal of the Mechanics and Physics of Solids* **193**, 105864 (2024).

[45] J. Rozman and J. M. Yeomans, *Physical Review Letters* **133**, 248401 (2024).

[46] P. Yu, R. Zhang, and B. Li, *Physical Review Letters* **135**, 108401 (2025).

[47] P. Yu and B. Li, *Acta Mechanica Sinica* **40**, 623297 (2024).

[48] C. Fang, J. Yao, Y. Zhang, and Y. Lin, *Biophysical Journal* **121**, 1266 (2022).

[49] S.-Z. Lin, D. Bi, B. Li, and X.-Q. Feng, *Journal of The Royal Society Interface* **16**, 20190258 (2019).

[50] S. Tong, N. K. Singh, R. Sknepnek, and A. Košmrlj, *PLoS Computational Biology* **18**, e1010135 (2022).

[51] S. Tong, R. Sknepnek, and A. Košmrlj, *Physical Review Research* **5**, 013143 (2023).

[52] C. Duclut, J. Paijmans, M. M. Inamdar, C. D. Modes, and F. Jülicher, *Cells & Development* **168**, 203746 (2021).

[53] D. Grossman and J.-F. Joanny, *Physical Review Research* **7**, 013039 (2025).

[54] X. Yin, Y.-Q. Liu, L.-Y. Zhang, D. Liang, and G.-K. Xu, *Nano Letters* **24**, 3631 (2024).

[55] E. Makhija, D. S. Jokhun, and G. V. Shivashankar, *Proceedings of the National Academy of Sciences of the United States of America* **113**, E32 (2016).

[56] A. Singh, T. Saha, I. Begemann, A. Ricker, H. Nüsse, *et al.*, *Nature Cell Biology* **20**, 1126 (2018).

[57] M. Uwamichi, H. Li, Z. Zhao, Y. Yao, H. Higuchi, K. Kawaguchi, and M. Sano, *Experimental identification of force, velocity, and nematic order relationships in active nematic cell monolayers* (2024), arXiv:2402.16151v1 [cond-mat.soft].

[58] S. Tlili, J. Yin, J.-F. Rupprecht, M. A. Mendieta-Serrano, G. Weissbart, N. Verma, X. Teng, Y. Toyama, J. Prost, and T. E. Saunders, *Proceedings of the National Academy of Sciences of the United States of America* **116**, 25430 (2019).

[59] S.-Z. Lin, M. Merkel, and J.-F. Rupprecht, *The European Physical Journal E* **45**, 4 (2022).

[60] T. B. Saw, A. Doostmohammadi, V. Nier, L. Kocgozlu, S. Thampi, Y. Toyama, P. Marcq, C. T. Lim, J. M. Yeomans, and B. Ladoux, *Nature* **544**, 212 (2017).

[61] K. Kawaguchi, R. Kageyama, and M. Sano, *Nature* **545**, 327 (2017).

[62] L. Balasubramaniam, A. Doostmohammadi, T. B. Saw, G. H. N. S. Narayana, R. Mueller, T. Dang, M. Thomas, S. Gupta, S. Sonam, A. S. Yap, *et al.*, *Nature Materials* **20**, 1156 (2021).

[63] C. Blanch-Mercader, V. Yashunsky, S. Garcia, G. Duclos, L. Giomi, and P. Silberzan, *Physical Review Letters* **120**, 208101 (2018).